Realia et naturalia

DISSERTATIONES
CHIMICAE
UNIVERSITATIS
TARTUENSIS
125

ANN LAHEÄÄR

Electrochemical characterization of alkali metal salt based non-aqueous electrolytes for supercapacitors

DISSERTATIONES CHIMICAE UNIVERSITATIS TARTUENSIS
125

DISSERTATIONES CHIMICAE UNIVERSITATIS TARTUENSIS
125

ANN LAHEÄÄR

Electrochemical characterization of alkali metal salt based non-aqueous electrolytes for supercapacitors

UNIVERSITY OF TARTU
PRESS
1632

Institute of Chemistry, Faculty of Science and Technology, University of Tartu, Estonia

Dissertation is accepted for the commencement of the degree of Doctor of Philosophy in Chemistry on June 11th, 2013 by the Council of the Institute of Chemistry, University of Tartu

Supervisors: Prof. Enn Lust, University of Tartu, Estonia
Ph.D. Alar Jänes, University of Tartu, Estonia

Opponent: Prof. Thierry Brousse, Université de Nantes, France

Commencement: August 23rd, 2013 at 10 a.m.
14a Ravila Street (Chemicum), auditorium 1021

ISSN 1406–0299
ISBN 978–9949–32–327–2 (print)
ISBN 978–9949–32–328–9 (pdf)

University of Tartu Press
www.tyk.ee
Order No. 265

TABLE OF CONTENTS

I. LIST OF ORIGINAL PUBLICATIONS

I. **A. Laheäär**, A. Jänes, E. Lust, $NaClO_4$ and $NaPF_6$ as potential non-aqueous electrolyte salts for electrical double layer capacitor application, Electrochimica Acta 82 (2012) 309–313.

II. **A. Laheäär**, A. Jänes, E. Lust, Lithium bis(oxalato) borate as an electrolyte for micromesoporous carbide-derived carbon based super-capacitors, Journal of Electroanalytical Chemistry 669 (2012) 67–72.

III. **A. Laheäär**, A. Jänes, E. Lust, Electrochemical properties of carbide-derived carbon electrodes in non-aqueous electrolytes based on different Li-salts, Electrochimica Acta 56 (2011) 9048–9055.

IV. **A. Laheäär**, A. Jänes, E. Lust, Electrochemical Behavior of Carbide Derived Carbons in $LiPF_6$ and $LiCF_3SO_3$ Nonaqueous Electrolytes, ECS Transactions 28(8) (2010) 65–75.

V. **A. Laheäär**, H. Kurig, A. Jänes, E. Lust, $LiPF_6$ based ethylene carbonate – dimethyl carbonate electrolyte for high power density electrical double layer capacitor, Electrochimica Acta 54 (2009) 4587–4594.

Author's contribution

Paper I: Performed all electrochemical measurements and analysis of data. Mainly responsible for the preparation of the manuscript.

Paper II: Performed all electrochemical measurements and analysis of data. Mainly responsible for the preparation of the manuscript.

Paper III: Performed all electrochemical measurements and analysis of data. Mainly responsible for the preparation of the manuscript.

Paper IV: Performed all electrochemical measurements. Participated in the analysis of data and preparation of the manuscript.

Paper V: Performed all electrochemical measurements. Participated in the analysis of data and preparation of the manuscript.

2. ABBREVIATIONS AND SYMBOLS

$|P|/|S|$ – normalized real part of complex power
$|Q|/|S|$ – normalized imaginary part of complex power
2TC – 2-electrode test cell
3TC – 3-electrode test cell
A – constant phase element coefficient
ac – alternating current
A_{cs} – molecular cross-sectional area of adsorbate
AN – acetonitrile
av – alternating voltage
BET – Brunauer-Emmett-Teller
c – BET theory constant
C – total system capacitance
C(Mo_2C) – carbon synthesized from Mo_2C
C(TiC) – carbon synthesized from TiC
C' – real part of capacitance
C'' – imaginary part of capacitance
C_1, C_2 – single electrode capacitances in a device
C_1/C_n – ratio of discharge capacitances of 1st and nth cycle
C_{CCCD} – capacitance from CCCD
CCCD – constant current charge/discharge
CDC – carbide derived carbon
C_{dif} – differential capacitance of electrode
C_{dl1} – external double layer capacitance
CE – counter electrode
C_{film} – resistive film capacitance
C_g – gravimetric capacitance per one electrode
CPE_2 – constant phase element
C_s – series capacitance
CV – cyclic voltammogram
C_{WE} – working electrode capacitance in a 3-electrode test cell
d – pore width
D – disorder-induced Raman peak
D*, G* – second-order Raman peaks
dc – direct current
DMC – dimethyl carbonate
E – working electrode potential
$E(t)$ – ac voltage function
E_0 – maximum amplitude of the av signal
EC – ethylene carbonate

$E_C(t)$ – voltage function over capacitance
EDL – electrical double layer
EDLC – electrical double layer capacitor
EIS – electrochemical impedance spectroscopy
E_{max} – maximum energy density
E_{OX} – oxidation potential (vs. Li/Li^+)
$E_R(t)$ – voltage function over resistance
f – frequency
$f(d)$ – pore size distribution function
f_R – relaxation frequency
G – graphite Raman peak
I – constant current
i – current
$I(t)$ – ac current function
I_0 – maximum amplitude of current
I_c – capacitive current
j – current density
j – imaginary unit
l – thickness of EDL
LIB – Li-ion battery
LIC – Li-ion capacitor
M – molarity
m_{ad} – adsorbent mass
m_{el} – mass of two electrodes
m_{WE} – mass of WE
n – number of transferred electrons
$N(P/P_0)$ – experimental adsorption isotherm data
$N(P/P_0,d)$ – isotherm corresponding to a pore of size d
N_A – Avogadro constant
NaIB – Na-ion battery
NaIC – Na-ion capacitor
NLDFT – non-local density functional theory
P – pressure
$P(\omega)$ – real part of complex power
P/P_0 – relative pressure
PC – propylene carbonate
P_{max} – maximum power density
PSDM – pore size distribution maximum
q – quantity of charge
$Q(\omega)$ – imaginary part of complex power
QSDFT – quenched solid density functional theory

R – ideal gas constant
R – resistance
R_1 – high frequency series resistance
RC – resistance–capacitance transmission line circuit
R_{ct1} – external charge transfer resistance
R_{ct2} – internal charge transfer resistance
RE – reference electrode
R_{film} – resistive film resistance
R_s – series resistance
S – electrode surface area
$S(\omega)$ – complex power
S_{BET} – specific surface area calculated from BET theory
SC – supercapacitor
SEI – solid electrolyte interface
S_{el} – cross-sectional surface area of electrode
S_{ext} – external surface area of adsorbent
SHE – standard hydrogen electrode
S_m – micropore area of adsorbent
S_{WE} – working electrode cross-sectional surface area
T – temperature
t – time
TC – test cell
T_m – melting point
t_{stat} – statistical adsorbed layer thickness
V_{ads} – volume of adsorbed adsorbate
V_m – micropore volume
V_{mol} – molar volume of adsorbate
W – mass of adsorbed gas
WE – working electrode
W_m – mass of adsorbate in a monolayer
Z – complex impedance
Z' – real part of impedance
Z'' – imaginary part of impedance
Z_{CPE} – constant phase element impedance
Z_w – Warburg-like diffusion impedance
ΔE – cell potential
$\Delta E(t)$ – potential response at CCCD
ΔE_d – potential delay
α_{CPE} – CPE fractional exponent
α_W – Warburg fractional exponent
γ-BL – γ-butyrolactone

ε – dielectric constant (25 °C)
ε_0 – dielectric permittivity of vacuum
ε_r – relative dielectric permittivity of electrolyte
η – viscosity
θ – phase angle
λ – ac penetration depth
λ_L – Raman operating wavelength
μ – dipole moment
ν – potential scan rate
σ_{ads} – Warburg constant
τ_R – characteristic time constant
ω – angular frequency

3. INTRODUCTION

Supercapacitors (SCs), also known as electrical double layer capacitors (EDLCs), ultracapacitors, or electrochemical capacitors, are high-power energy storage devices [1–8]. Energy is stored in SCs through reversible physical adsorption of electrolyte ions on the interface between large surface area polarized electrode and electrolyte, i.e. formation of the electrical double layer (EDL). Physical charge storage mechanism enables quick charging and discharging of the device (in seconds), high cycle life (> 100,000 cycles), and good electrical efficiency (> 95%), differently from most rechargeable battery designs, where chemical energy is stored through rather slow and partly non-reversible charge-transfer reactions, often accompanied by phase change. However, due to electrostatic surface interactions in SCs, the energy density is smaller compared to the energy content of bulk reactions in batteries [9–11].

Various porous materials, electrolytes and separator materials are being prepared and electrochemically characterized with the aim to improve the performance of SCs. Micro-meso-porous carbon electrodes demonstrate high power, moderate energy density and good cycle life in electrolytes of quaternary alkylammonium salts in acetonitrile (AN), and somewhat lower power with propylene carbonate (PC) or γ-butyrolactone (γ-BL) based electrolytes, i.e. in electrolytes also used in commercial SCs [4, 7, 12–14]. Finding a replacement for electrolytes based on harmful AN or viscous PC and γ-BL (also psychotropic) is an important step for wider commercialization of SCs. For example, environmentally friendlier ethylene carbonate and dimethyl carbonate mixed solvent system (1:1 by volume) is proposed in this thesis. In addition to changing the solvent, possible electrolyte salt candidates have to be studied to establish a solvent/salt combination characterized by good electrochemical stability, fast mass transfer, high degree of adsorption, etc. Alkali metal salts, especially Li-salts, have already been successfully used and are still under studies for different battery designs [15–21]. As World's economically viable Li resources are limited, alternative electrolyte cations are being searched for. The electrolyte salts chosen in this study, as possible candidates for SC application, include four lithium salts containing hexafluorophosphate (PF_6^-), perchlorate (ClO_4^-), trifluoromethanesulfonate ($CF_3SO_3^-$) or bis(oxalato)borate ($B(C_2O_4)_2^-$) anions; two sodium salts containing PF_6^- or ClO_4^- anions, and cesium carborane ($Cs^+CB_{11}H_{12}^-$) for comparison. The electrochemical characteristics such as maximum applicable cell potential (stability under polarization), mass transfer resistance, charging-discharging time constants, EDL capacitance with accompanying specific adsorption or intercalation, energy and power capability, etc., were analyzed in relation to the ionic composition of the electrolyte.

Non-linear least squares fitting method was applied on the experimental electrochemical impedance spectroscopy data for a better understanding of the complex mixed kinetic resistive and capacitive processes taking place at the electrode/electrolyte interface. Also, with real application purposes, time stability test were done for some of the more perspective SCs under study.

4. LITERATURE OVERVIEW

4.1. Supercapacitors

Supercapacitors as devices storing energy in the electric field of EDL have been studied since 1950s with the first patent dating from 1957 [22]. Different carbon materials with high surface area and open porosity are mainly used as electrode materials, giving high volumetric and gravimetric capacitance in either aqueous or non-aqueous electrolytes [1–3]. However, the term 'supercapacitor' covers also devices where, in addition to EDL formation, pseudocapacitive redox processes take place, originating either from the electrode material (metal oxides, conductive polymers, chemically modified carbons, intercalation compounds), from electrochemically active electrolyte, or from reversible hydrogen electrosorption in porous carbons [1, 2, 23–30]. In this study the focus is on SCs based on carbon materials and electrolytes with classical EDL formation and no remarkable pseudocapacitive contribution.

Similarly to traditional electrolytic capacitors, cations and anions within the electrolyte accumulate (are adsorbed) at the surface of solid electrode of opposite charge to compensate for the electronic charge at the electrode surface. The advantage of SCs is the much higher capacitance of electrodes (and thus energy density of the device) due to the extremely large internal effective surface of the porous electrode materials and the small thickness of EDL (in the order of 3–10 Å), expressed by Equation (1):

$$C_{\mathrm{dif}} = \frac{S\varepsilon_0\varepsilon_{\mathrm{r}}}{l}, \tag{1}$$

where C_{dif} is the differential capacitance of electrode, S is the surface area and l is the thickness of EDL, ε_0 is the dielectric permittivity of vacuum, and ε_{r} is the relative dielectric permittivity of electrolyte [4, 31]. However, power density of SCs is somewhat lower due to hindered ion mass transfer in the small pores of the electrode matrix.

A single-cell SC device consists of two thin electrode layers with an electrically insulating ion-permeable separator in between, all soaked with electrolyte and pressed together between ideally polarizable current collectors (Figure 1).

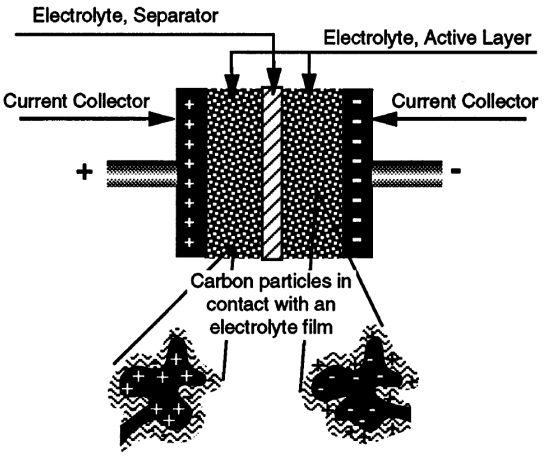

Figure 1. Principle of a single-cell supercapacitor [4].

The two electrodes in a SC single-cell are connected in series and in ideal case have exactly equal capacitances ($C_1 = C_2$). Thus, the overall device capacitance C can be expressed by Equation (2) through the capacitances of single electrodes, C_1 and C_2:

$$\frac{1}{C} = \frac{1}{C_1} + \frac{1}{C_2}. \tag{2}$$

It follows from Equation (2) that the overall capacitance of a symmetric SC device is half of the capacitance of a single electrode, and the gravimetric capacitance (F g^{-1}) of a real working device is one fourth of that of a single electrode [3]. It is also important to note that if C_1 and C_2 are not equal, the smaller capacitance mainly determines the device capacitance.

4.1.1. Electrical double layer theories, specific adsorption and intercalation of ions

The concept of an electrical double layer corresponds to a model consisting of two array layers of opposite charges, separated by a small distance having atomic dimensions, and facing each other [1, 2]. This model was adopted by Helmholtz first for the interface of colloidal particles and then adapted to electrode interfaces in 1853 [32]. It is the simplest EDL theory describing the EDL as two parallel charged layers, i.e. electrode surface region of excess positive or negative charge and a charge compensating layer of static electrically adsorbed counter-charge ions at a distance approximately equal to the solvent molecule diameter. EDL differential capacitance is described by Equation (1). Both layers are assumed to have uniform charge distribution, but

in reality this approximation could only be made to the electrode part of the EDL because adsorption effect depends strongly on the electrolyte concentration, ion and solvent nature, etc. [33, 34].

Some time after the Helmholtz model was proposed Gouy introduced a modified version in 1910 in which the thermal fluctuation of counterions was taken into consideration [35]. Instead of the so-called compact Helmholtz layer, the electron excess or deficit charge on the electrode surface is compensated by a layer of diffusively distributed cation and anion population having an equal but opposite net charge. A full mathematical treatment for this model was done by Chapman in 1913 [36], based on the combined application of Boltzmann's energy distribution equation and Poisson's equation. Due to the treatment of ions as point charges in the so-called diffuse layer, interpretation of the EDL was erroneous on account of an incorrect potential profile and local field near the electrode surface, and consequently an overestimation of the EDL capacitance [1].

The next stage of development in the EDL theory by Stern in 1924 [37] treated the inner region of ion distribution in terms of adsorption process according to Langmuir's adsorption isotherm (so-called Helmholtz layer), and the outer layer in terms of diffuse region as in Gouy and Chapman theories. The compact adsorption layer had now a defined geometrical limit determined by the size of ions with their solvation shell, and therefore the EDL capacitance was no longer overestimated, being inversely dependent on the EDL thickness. Stern also recognized that a satisfactory theory of the EDL must take into account any specific chemisorption interactions that ions may experience with the electrode surface [1].

In 1940s, Grahame made important improvements in the EDL theory by differentiating the inner and outer Helmholtz layer regions, taking into account the different closest approach of anions and cations to the electrode surface [38], maintaining of course the diffuse layer. Depending on the electrode material (different metals, carbon of various surface chemistry, etc.), electrolyte cation and anion sizes and solvent nature, some ions can approach closer to the electrode surface and form the so-called inner Helmholz layer by (partly) losing their solvation shell. Partial charge transfer from strongly polarizable adsorbed ions (more commonly anions) can occur, i.e. specific adsorption. The outer Helmholtz layer is formed by ions that retain their solvation shell and do not adsorb specifically [1].

In addition to the discussed EDL models, there are several modern interpretations like Rice, Thomas-Fermi, modified Thomas-Fermi, Hurwitz-Parsons, Kornyshev, etc., taking into account the non-ideality of electrode surface, i.e. potential drop inside the electrode surface layer, the specifics and different interactions of adsorbed ions, and other additional phenomena in the EDL [39–47].

When specific adsorption occurs like described in the Grahame theory, the charge of the inner Helmholtz layer, opposite to that on the electrode surface,

might exceed that of the electrode. Such strong specific effect causes reversals in the direction of EDL potential profile [38]. Specific adsorption of halide ions on bismuth single crystal planes has been demonstrated with the strongest effect established for I^- ions in aqueous and non-aqueous electrolytes [48, 49]. Weak specific adsorption effect was also observed for ClO_4^- anions in aqueous electrolyte [50]. The influence of specific adsorption of bulky tetraalkyl-ammonium cations on the charge-compensation mechanism in carbon micropores, together with the effect of coupling confined specific adsorption of cations and charge-induced desorption of anions, has been analyzed by Levi et al [51].

When using graphitic materials, or also amorphous carbons with some graphitic areas, the possibility of intercalation of electrolyte anions at the positively charged electrode and cations at the negatively charged electrode have to be taken into account [1]. Intercalation could be considered as one form of specific adsorption, where similarly to specific surface adsorption partial charge transfer might occur from ion to electrode surface. Beck and Krohn studied the reversible intercalation and deintercalation of anions at highly crystalline graphite electrodes [52], and the intercalation of cations has also been thoroughly examined, being the basis of Li-ion battery (LIB) technology [16].

When considering Li^+ ion intercalation (or probably also Na^+, Cs^+, etc.) from non-aqueous electrolytes, solid electrolyte interface (SEI) formation and its properties are a key factor. Complicated electroreduction reaction kinetics develops during the first cathodic polarization cycle of graphite (or partly graphitized carbon) electrode in a non-aqueous lithium salt solution, and at electrode potential $E < 1.0$ V (vs. Li/Li^+ reference electrode) Li^+ ions intercalate into graphite in parallel with the reduction of solvent molecules [15, 18, 53–55]. When solvent reduction process occurs within the graphite particles, the graphite structure is damaged (expanded) and electrode loses electrical conductivity and mechanical stability. However, if the surface reduction processes (Li^+ and solvent molecule reduction) are fast enough in comparison with absorption, mass transfer and charge transfer processes between graphite layers, a thick surface film forms which blocks the co-intercalation of solvent molecules with Li^+ ions and prevents further destructive reduction processes inside the graphite particles [56].

4.2. Carbon as electrode material

Carbon is a unique material due to its possible existence as different allotropes (graphite, graphene, nanotubes, fullerenes, amorphous carbon, diamond, etc.) and in various microtextures of different dimensionality (from 0 to 3D) and geometrical forms (powders, foams, fabrics, felts, etc.), which makes it an attractive material for electrochemical energy storage and other novel

technologies. Carbon electrodes have good polarizability, high electrical conductivity, good thermal, chemical and electrochemical stability (corrosion resistance), easy processability, etc. Porous carbon can be synthesized by simple physicochemical methods from various easily attainable natural precursor materials (coconut shell, wood, different hydrocarbons), i.e. by carbonization process and subsequent activation to get the so-called activated carbon; from carbides by selective etching to form carbide derived carbon (CDC); from organic aerogels by pyrolysis to obtain carbon aerogel; etc. Carbon is an environmentally friendly material and of rather low cost, however, noticeably depending on the raw materials and synthesis technologies applied. The microtexture can be tuned by the choice of precursor material/compound, synthesis conditions, thermal and chemical post-treatment, giving carbons with surface area of up to ~2500 $m^2 g^{-1}$ [1–5, 57–61].

The majority of commercial carbons used today have an amorphous structure that can be considered as sections of hexagonal carbon layers with very little order parallel to the layers. The conductivity of solid carbons is strongly influenced by heat treatment temperature, depending on the precursor material and synthesis method. The intra-particle resistivity is dependent on the chemical and structural morphology of carbon, but the electrical resistance of a packed carbon electrode is a function of both its intra-particle resistance and the contact (or inter-particle) resistance [62]. For a porous carbon matrix, resistance on the current-carrying path involves moving through the carbon particle, across the carbon/carbon and carbon/current collector interfaces, and through the metallic collector [3].

Studying the effect of the pore size distribution on the capacitance of porous carbon electrodes has shown that by increasing the specific surface area, capacitance enhancement can be achieved to a certain extent; however, it is more important to optimize the pore size of the material, taking into account the electrolyte characteristics [58, 59]. Experimental data confirms that pores of sizes smaller than solvated ions in the electrolyte, contribute noticeably to the capacitance, i.e. (partial) solvation shell removal occurs during adsorption onto/into micropores [5, 12–14, 59, 63–67]. Inaccuracy in correlating electrode differential capacitance with measured surface area can arise also from the assumption that the surface accessed by N_2 or CO_2 molecules is similar to the surface accessed by electrolyte during the measurement of differential capacitance. In addition, wettability and pseudocapacitive phenomena are not considered during surface area estimation by gas sorption data [3].

4.2.1. Carbide derived carbon (CDC)

The advantage of CDC materials is a unique pore size distribution with pore dimensions being accurately tunable [23, 63–69]. High-temperature etching in halogens is the prevalent synthesis method, but CDCs can be produced also by leaching in supercritical water, high-temperature decomposition, and vacuum

decomposition [23]. Various nanostructures, degree of graphitization and amorphous structure, and different pore size distributions of CDCs can be practically achieved by varying the precursor carbide (TiC, SiC, Mo_2C, VC, Al_4C_3, Cr_xC_y, WC, etc.) and thermal conditions of extracting the carbideforming element from the crystal lattice of the carbide used [64–71]. The micropore formation is influenced by the initial carbide density, but mesopore formation is rather influenced by carbide structure and chemical properties and not carbide density [72].

CDC synthesis by chlorination is represented by Equation (3):

$$XC_x + \frac{y}{2}Cl_2 \overset{t^\circ}{=} XCl_y + xC, \tag{3}$$

where X is the carbide forming element in the carbide lattice (e.g. Ti, Si, Mo, etc.). The obtained carbon might be additionally treated with an oxidizer (e.g. water vapor or CO_2) to open closed pores. High-temperature (e.g. 800 °C) H_2 (or mixture with an inert gas) treatment during a few hours is necessary to remove residual chlorine, chlorides and oxygen-containing functional groups from the surface of porous carbon [64–67].

4.2.2. Gas sorption for carbon porosity characterization

N_2 and CO_2 adsorption at 77 K and 273 K, respectively, are mainly used for the characterization of the porous structure of different materials, sometimes also Ar or Kr. CO_2 adsorption is preferred for accurate determination of the so-called ultramicroporosity (pores of diameter < 1 nm) of carbon materials. According to the IUPAC nomenclature, micropores are of a diameter < 2 nm, mesopores in the range from 2 nm to 50 nm, and macropores larger than 50 nm. Sometimes the term ‘nanopores’ is also used for pores of diameter ≤ 2 nm, which reflects their actual size more appropriately [23].

4.2.2.1. Brunauer-Emmett-Teller (BET) theory

BET method is a widely used method for determining the specific surface area of adsorbents, catalysts and various other finely divided and porous materials [73]. The BET equation is written as:

$$\frac{1}{W((P/P_0)-1)} = \frac{1}{W_m c} + \frac{c-1}{W_m c}\left(\frac{P}{P_0}\right), \tag{4}$$

where W is the mass of gas adsorbed at a relative pressure of P/P_0, W_m is the mass of adsorbate in a monolayer. BET theory constant c is related to the

adsorption energy of the first adsorbed layer, i.e. describes the interaction energy between adsorbent and adsorbate molecules. Thus, BET plot of $1/W((P_0/P)-1)$ versus P/P_0 should be linear. For most materials, a linear relation occurs in the P/P_0 range from 0.05 to 0.35 (for microporous materials up to ~0.2) on N_2 adsorption isotherms. Generally a multi-point BET method is used for which at least three adsorption/desorption points are needed within the appropriate pressure range [74].

W_m can be calculated by combining the slope s and intercept i of the BET plot from Equation (5) in Equation (6):

$$s = \frac{c-1}{W_m c},\ i = \frac{1}{W_m c}, \tag{5}$$

$$W_m = \frac{1}{s+i}. \tag{6}$$

The specific surface area S_{BET} of a material can be calculated using W_m according to Equation (7):

$$S_{BET} = \frac{W_m N_A A_{cs}}{M m_{ad}}, \tag{7}$$

where N_A is the Avogadro constant ($6.023 \cdot 10^{23}$ molecules per mole), A_{cs} is the molecular cross-sectional area of adsorbate (A_{cs} = 1.62 nm^2 for N_2 at 77 K [75]), M is the molecular weight of adsorbate molecule, and m_{ad} is the adsorbent mass, i.e. mass of the sample [74].

4.2.2.2. Calculation of total pore volume

Total pore volume is calculated from the adsorption data at a relative pressure as close to unity as possible, where an approximation can be made of all pores being filled by the condensed adsorbate [76]. At a pressure P and temperature T, the total pore volume V_t is expressed as:

$$V_t = \frac{P V_{ads} V_{mol}}{R\ T}, \tag{8}$$

where V_{ads} is the volume of adsorbed adsorbate, V_{mol} is the molar volume of adsorbate (34.7 $cm^3\ mol^{-1}$ for N_2 at 77 K), and R is the ideal gas constant (8.314 $J\ mol^{-1}\ K^{-1}$).

4.2.2.3. The *t*-plot method

The *t*-plot method extends to higher relative pressures compared to the BET method and therefore enables determining the so-called external surface area S_{ext} of the adsorbent material, i.e. meso- and macroporous surface [74, 76]. The adsorbed gas volume V_{ads} is plotted against the statistical adsorbed layer thickness t_{stat} to obtain the so-called *t*-plot. There are several calculation methods to determine t_{stat} [77–80]. A convenient t_{stat} calculation method by de Boer [77] is widely used:

$$t_{stat} = \sqrt{\frac{13.99}{\log(P/P_0) + 0.034}} \,. \tag{9}$$

The *t*-plots for materials containing micropores tend to deviate from linear shape at lower relative pressures. S_{ext} can be calculated from the slope *s* of the linear high-pressure part of the curve according to:

$$S_{ext} = 15.47s \,, \tag{10}$$

where 15.47 is the density conversion factor for N_2. In the absence of micropores there is good agreement between S_{ext} and S_{BET}.

In case of partly microporous materials, the micropore volume V_m can be calculated by extrapolating the high-pressure linear plot to the V_{ads} axis, giving a positive intercept *i* equivalent to V_m:

$$V_m = 0.001547i. \tag{11}$$

The micropore area S_m of adsorbent can be found from the difference of S_{BET} (total area) and S_{ext} (meso- and macropore area):

$$S_m = S_{BET} - S_{ext} \,. \tag{12}$$

4.2.2.4. Non-local density functional theory (NLDFT)

NLDFT theory [81, 82] is a method for determining the pore size distribution of different materials. The classical theories like Dubinin-Radushkevich [83] and Barret-Joyner-Halenda [84] and semi-empirical methods like Horwath-Kawazoe [85] do not describe realistically the filling of micropores and smaller mesopores with adsorbate. NLDFT describes objectively the local structure of condensed adsorbate at solid curved surfaces. The shape of adsorption isotherms for model pores is determined by the liquid-liquid and liquid-solid interactions. A relation between such isotherms from a microscopic approach

and the experimental isotherms for porous solids can be given by the generalized adsorption isotherm (GAI) equation:

$$N(P/P_0) = \int_{d_{\min}}^{d_{\max}} N(P/P_0, d) f(d) \mathrm{d}d \,, \tag{13}$$

where $N(P/P_0)$ is the experimental adsorption isotherm data, d is pore width, $N(P/P_0,d)$ is an isotherm corresponding to a pore of size d, and $f(d)$ is the pore size distribution function. The GAI equation assumes that the experimental isotherm consists of isotherms of single pores multiplied by their relative distribution $f(d)$ over the range of pore sizes [81, 82].

Recently, an improved theory called the quenched solid density functional theory (QSDFT) has been worked out for determining the micro- and mesopore volumes and pore size distribution [86, 87].

4.3. Electrolytes for supercapacitors

As the power and energy delivered by a SC device depend on a squared cell potential ΔE, it is an important SC characteristic to be optimized. As carbon electrode materials have good electrochemical stability, it is usually the electrolyte that determines the operating ΔE of SCs. Solvent stability slightly higher than the intended operational ΔE is preferable to avoid problems during occasional slight overcharge [1, 3, 4]. The thermodynamic decomposition potential of water is 1.23 V, thus together with ohmic losses the maximum applicable potential is ~1.0 V when using aqueous electrolytes, e.g. H_2SO_4, KOH, NaCl, NaF. Organic solvent based electrolytes allow applying potentials above 2.5 V, e.g. commercially employed alkyl ammonium salts in AN or PC. Some tested electrolytes even allow potentials of up to 4.0 V [1–4, 7, 12–14]. The need to prepare organic solvents and salts free from traces of electrochemically active water and oxygen, and having special clean and dry conditions for storing other SC components and for assembling SC systems, make non-aqueous SCs more expensive compared to aqueous systems.

The advantage of higher ΔE is slightly cancelled out by the higher viscosity of organic solvents and generally lower electrolyte concentrations, resulting in an order of magnitude lower electrolyte specific conductivity in comparison with aqueous electrolytes. The salt concentration in a specific solvent should be optimized to minimize the formation of ion-pairs with the accompanying decrease in conductivity. The capacitance of high surface area carbons is generally higher in aqueous electrolytes owing to the higher dielectric constant of water (~80 for H_2O vs. ~36 for AN, and ~65 for PC). The size of solvation shell and the ability of ions to partly or entirely lose the solvation shell during adsorption depend strongly on the combination of electrolyte salt and solvent

(or a mixture of solvents). All these factors determine the mobility of dissociated ions and the concentration of free charge carriers, i.e. the specific conductance of electrolyte [1–4]. In addition, practical electrolytes should be non-toxic to be accepted environmentally for ease of handling, mass production, and waste treatment [16].

Ionic liquids (IL), i.e. salts with melting point below 100 ºC, are widely studied as SC electrolytes due to their negligible vapor pressure and theoretically much higher electrochemical stability (up to 5 V) of some ILs compared to molecular liquids [88–90]. Unfortunately, most ILs have low electrical conductivity (< 5 mS cm^{-1}) and high viscosity (> 50 mPa s), or a narrow region of electrochemical stability [88]. The choice of ILs is wide and the electrochemical characteristics depend strongly on the IL ionic composition and operating temperature [88, 91, 92]. In reality, the limiting cell potential of an IL based SC device is similar as in case of non-aqueous electrolytes (< 3.5 V). Also, despite the higher bulk conductivity of ILs at elevated temperatures, the ILs tend to decompose under polarized conditions, and the adsorption equilibrium is shifted towards desorption [92].

4.3.1. Alkali metal salts in a carbonate solvent mixture

Organic carbonates have been successfully used for LIBs as mixed solvent systems in different combinations over a few decades already [16], and a cyclic carbonate, PC, has been applied also in commercial SCs [3]. Such organic solvents are attractive candidates for SCs due to their suitable physical and electrochemical properties (Table I) and reduced harmfulness to the environment or human beings, compared to other commercially applied electrolyte solvents (AN and γ-BL).

A practical electrolyte should retain good conductivity over a wide temperature range, e.g. from –40 to 70 °C. Usually, below 0.4 M electrolyte salt concentration the conductivity decreases markedly, and above 1 M concentration there is significant salt precipitation at low temperatures. Generally, electrolytes with a single carbonate solvent cannot provide all the requirements of a practical electrolyte. The high-viscosity cyclic carbonates are often mixed with linear carbonates to lower the viscosity and increase ionic conductivity of the electrolyte [1, 16, 93, 94].

The solvent mixture chosen in this thesis for electrochemical testing of different salts is ethylene carbonate (EC) and dimethyl carbonate (DMC) mixture of equal volumes. The advantages of the cyclic carbonate EC are its high dielectric constant ε and dipole moment μ, but EC is solid at ambient temperature (Table I), so it could not be used alone. The linear DMC is a low-viscosity liquid, but oppositely to EC, it has small ε and μ. Both EC and DMC have higher electrochemical stability, i.e. oxidation potential, compared to PC and AN [16]. Although the conductivity of DMC based electrolytes is very poor below –10 °C and that of EC based electrolytes negligible below 30 °C, it has

been shown in several studies that the conductivity of 1 M solutions of different salts is higher in a wide temperature range (–40 to 50 °C) in EC:DMC solvent mixture, or some other solvent combinations (e.g. with ester additions), compared to PC due to its high viscosity [16, 93, 94].

Table I. Physical characteristics and electrochemical stability of non-aqueous solvents [16].

Solvent	T_m / ºC	ε	μ / D	η / mPa s	E_{OX} / V
EC	36.5	90 (40 °C)	4.87	1.9 (40 °C)	5.2
DMC	3	3.1	0.88	0.59	5.1
PC	–54.5	65	4.98	2.51	4.3
AN	–48.8	36	3.44	0.34	3.8

T_m – melting point; ε – dielectric constant (25 °C); μ – dipole moment; η – viscosity; E_{OX} – oxidation potential (vs. Li/Li^+).

First, Li-salts were tested in this study, in the example of LIBs [16–21] to test their applicability in SCs, and to compare the effect of various anions in the salt composition on the electrochemical characteristics and stability under SC operational conditions [95–98]. The SEI formation has been shown to be inefficient in preventing solvent co-intercalation in most PC solvent and Li-salts based electrolytes [56]. However, stable SEI was demonstrated in $LiB(C_2O_4)_2$ solution in PC while supporting reversible lithium ion intercalation [99]. Also, $LiB(C_2O_4)_2$ electrolyte can stabilize aluminum to more positive potentials and is itself thermally more stable than $LiPF_6$ [21, 100]. Marom et al demonstrated that aluminium does not reach good passivation above 4.2 V vs Li/Li^+ in $LiClO_4$ solutions, whereas effective passivation is observed with $LiPF_6$ electrolyte even at higher potentials than 5 V vs Li/Li^+ [18]. $LiPF_6$ electrolyte in EC:DMC mixture has been studied before for hybrid capacitor with graphite negative and activated carbon positive electrode [101]. This is also the most commonly applied electrolyte in Li-ion capacitors (LIC) that has become an extensively studied class of SCs, where many different Li-ion doping materials are developed to achieve high-energy SCs [102–104]. Due to the limited economically viable World's lithium resources, two attainable Na-salts were also tested in this study, with the same anions in the composition as in the tested Li-salts [105, 106]. Differently from lithium, sodium cannot be reversibly intercalated into graphite, but the development of so-called Na-ion capacitors (NaIC) and Na-ion batteries (NaIB) was resumed when Na-ion insertion into hard carbon was established [107]. Solid state nuclear magnetic resonance studies have been done to verify and analyze the Na-ion intercalation into hard carbons [108]. Similarly to LICs, Na-ion pre-doping of hard carbons has been tested to prepare NaICs [109] and NaIBs [110, 111]. The electrochemical behavior of an uncommon Cs-salt based electrolyte was analyzed for a more comprehensive comparison in this thesis.

4.4. Separators in supercapacitors

The role of separator (also called membrane) in supercapacitors as well as other energy storage devices (batteries and fuel cells) is to prevent the device from short-circuiting due to direct mechanical contact between oppositely charged electrodes, whereas enabling free ionic transport. Usually thin layers of highly porous or fibrous polymer materials are applied. There are various properties that determine the suitability of a separator. It has to be chemically and electrochemically stable towards electrolyte and electrode materials, as thin as possible to minimize the internal resistance of the device while maintaining mechanical strength, and permeable to solvated electrolyte ions (suitable porosity) [4, 112]. The wettability of separators by electrolytes of different chemical composition and viscosity varies widely and has strong influence primarily on the power performance of the SC device [112–114].

4.5. Methods for electrochemical characterization

4.5.1. Cyclic voltammetry

Cyclic voltammetry is an electrochemical method for estimating the potential limits and capacitance, for visualization and characterization of faradaic processes and other characteristics of SCs. The electrode potential is swept linearly between two fixed potential limits and a cyclic voltammogram (CV) is recorded, i.e. potential change versus current response of the studied system. Generally, potential scan rates $\nu = \pm \mathrm{d}E/\mathrm{d}t$ between 0.1 mV s^{-1} and 1 V s^{-1} are applied [1, 2, 4]. The current response i (A) of a SC with characteristic system capacitance C (F) is given as:

$$i = C\frac{\mathrm{d}E}{\mathrm{d}t} = C\nu. \tag{14}$$

Quite often C is a function of cell potential ΔE during charge or discharge cycle for carbon based SCs, faradaic pseudocapacitance devices and hybrid devices. Thus, the net charge during device cycling can be found by integration of CVs. The gravimetric capacitance C_{WE} (F g^{-1}) of the working electrode (WE) in a three-electrode test system is calculated from the system response current density j (A cm^{-2}) according to:

$$C_{\mathrm{WE}} = \frac{j\,S_{\mathrm{WE}}}{\nu\,m_{\mathrm{WE}}}, \tag{15}$$

where S_{WE} is the WE cross-sectional surface area (cm^2) and m_{WE} is the mass of WE (g).

Taking into account Equation (2), the gravimetric capacitance of a single electrode in a two-electrode SC device is expressed as:

$$C_g = \frac{4\, j\, S_{el}}{\nu\, m_{el}}, \tag{16}$$

where S_{el} is the cross-sectional surface area of electrodes (cm^2) and m_{el} is the mass of two electrodes (g) [98].

For an ideal capacitor, the CV has a rectangular shape (Figure 2). In real systems there is always resistance, making the CV decline slightly, and the mass transfer process related resistance in the porous carbon electrode matrix of SC devices cause a potential delay on the reversal of potential scan direction (charging to discharging and *vice versa*) (Figure 2). The peak on the curve 4 in Figure 2 is related to some pseudocapacitive redox reaction. Cyclic voltammetry is a useful method for describing the reversibility of different redox processes by the analysis of the potential difference between oxidation E_{OX} and reduction peak E_{RED} potentials (based on the Nernst equation the difference $E_{OX} - E_{RED} = 58/n$ mV for a reversible process of n electron transfer and of equal redox peak currents [115]). In case of partially reversible process, the distance is wider between redox peaks and the peak current intensity changes. For an irreversible process, only one peak occurs without the reverse process peak. For SCs with pseudocapacitance, the faradaic process might not have a narrow reduction/oxidation peak, but can influence the capacitance of a SC device in a wider potential range, i.e. the charging/discharging current is a continuous function of potential. Also, peaks can be caused by specific adsorption of some ions with partial charge transfer [1, 2, 4].

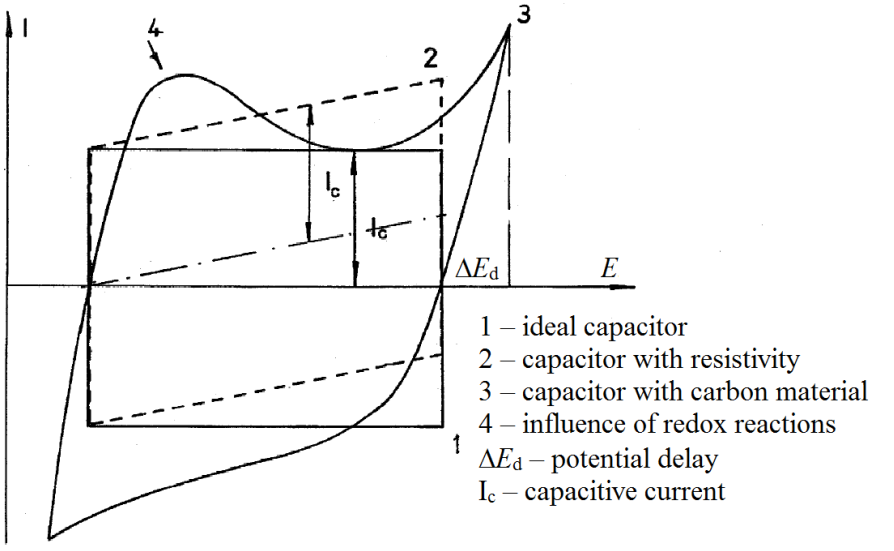

Figure 2. Typical voltammetry characteristics of a supercapacitor [57].

4.5.2. Electrochemical impedance spectroscopy

Electrochemical impedance spectroscopy (EIS) is a method for determining the frequency response of a capacitor device over a wide range of alternating current (ac) frequencies *f* from 1 mHz up to 100 kHz, or sometimes more. An ac signal generated by the system under study in response to an applied alternating voltage (av) is one of the most direct response functions that characterize the interfacial or pseudocapacitive behavior of an electrode. The method is especially valuable because it enables separate evaluation of the equivalent series resistance of electrode structure, overall device resistance, and any potential-dependent faradaic resistance caused by redox processes, and, depending on measurement conditions, also to distinguish pseudocapacitance from EDL capacitance [1, 2].

The parameters derived from an EIS spectrum fall generally into two categories [116]:

(a) those pertinent only to the material itself, such as conductivity, dielectric constant, mobility of charges, equilibrium concentrations of the charged species, and bulk generation/recombination rates; and

(b) those pertinent to an electrode/material interface, such as adsorption/ faradaic reaction rate constants, capacitance of the interface region, and diffusion coefficient of neutral species in the electrode itself.

EIS is based on a modulation function $E(t)$ expressed as [1, 12, 116]:

$$E(t) = E_0 \sin \omega t \,, \tag{17}$$

where E_0 is the maximum amplitude of the av signal, $\omega = 2\pi f$ is the angular frequency and *f* is the av frequency in Hz.

The current response $I(t)$ for a pure resistance is according to Ohm's law ($I = E/R$):

$$I(t) = I_0 \sin \omega t \,, \tag{18}$$

so that $I(t)$ is in phase with $E(t)$, i.e. related in the same way as for a direct current (dc) circuit, and I_0 is the maximum amplitude of current.

For a pure capacitive element/circuit, the instantaneous quantity of charge *q* on the capacitor during an applied av signal is:

$$q = CE(t) = CE_0 \sin \omega t \,, \tag{19}$$

from where the corresponding current response $I(t)$ can be found:

$$I(t) = \frac{\mathrm{d}q}{\mathrm{d}t} = C\frac{\mathrm{d}E(t)}{\mathrm{d}t} = \omega C E_0 \cos \omega t \,. \tag{20}$$

The applied av is a sinωt function and the response current of a capacitance is a cosωt function, and as cosωt = sin($\omega t + \pi/2$), the phase angle θ between the current and voltage signals is –90°. It follows from Equation (20) and Ohm's law that $1/\omega C$ must carry dimensions of resistance, but, unlike R, its magnitude falls with increasing frequency. Thus, the impedance of a capacitive element Z'', called the imaginary part of impedance, is expressed as:

$$Z'' = -\frac{1}{\omega C} \,. \tag{21}$$

According to Equations (17) and (18) and Ohm's law, the response signal of a resistive element, known as the real part of impedance, is expressed as:

$$Z' = R \,. \tag{22}$$

In a real SC device, there are both capacitive and resistive components and the overall system response to an applied av is a complex frequency-dependent signal. To the first approximation EDLC can be considered as resistance and capacitance in series. The voltage applied is a sum of the voltages over the resistance $E_R(t)$ and capacitance $E_C(t)$ connected in series:

$$E(t) = E_C(t) + E_R(t) \,. \tag{23}$$

Due to the phase angle between $E(t)$ and $I(t)$, a complex number notation (with imaginary unit $\mathrm{j} = \sqrt{-1}$) is introduced to simplify the representation of EIS signal, determining the signal of the capacitance as an imaginary part and of resistance as the real part of impedance. The current $I(t)$ is equal for elements connected in series, therefore the combination of Equations (17) to (23) gives:

$$E(t) = I(t)(R + \frac{1}{\mathrm{j}\omega C}) = I(t)Z \,, \tag{24}$$

where Z is the complex impedance:

$$Z = Z' + \mathrm{j}Z'' = R - \frac{\mathrm{j}}{\omega C} \,, \tag{25}$$

$$|Z|^2 = (Z')^2 + (Z'')^2 \,. \tag{26}$$

A typical *Z*',*Z*''-plot for a non-aqueous SC based on porous carbon electrodes is given in Figure 3, which can be divided into three distinguished sections when no faradaic reactions take place [1, 4, 7]. The micro-meso-porous carbon electrode behavior approximates to a planar electrode at low ac *f* range from ~0.1 to 0.001 Hz (i.e. at high ac penetration depth λ [7, 65, 117]), where the Nyquist plots are linear and practically vertical, indicating nearly ideal capacitive behavior with well developed 'knees' observed at ~0.1 Hz (Figure 3) [1, 4, 7]. The limiting process in this region is adsorption of ions at/into the micro-meso-porous carbon surface. In the moderate ac *f* range (~0.1 to ~50 Hz), λ is smaller than the length of pores, so the ac signal detects only a part of the pore volume. This part of Nyquist plots with a nearly –45° slope is called 'porous electrode section', where diffusion-like mass transfer process, i.e. Warburg semi-infinite diffusion or more complex mass transfer process, is the rate limiting step [12, 14, 65, 93, 117]. At higher *f* from ~100 to $3 \cdot 10^5$ Hz, there is a slightly depressed semicircle in the Nyquist plots that describes mixed kinetic adsorption and charge transfer processes at macroscopic heterogeneous electrode surface, as well as the formation and electrochemical behavior of a thin passive layer on the deposited Al current collectors [14, 65, 116–120]. The so-called total high-frequency series resistance R_s values can be obtained from Nyquist plots at $f \to \infty$. R_s consists of electrolyte resistance (including the wetting and permeability of the ion-conducting membrane), electrode material resistances and contact resistance between Al current collector (including thin passive layer) and porous carbon electrode ($R_s = R_{electrolyte} + R_{electrode} + R_{contact}$).

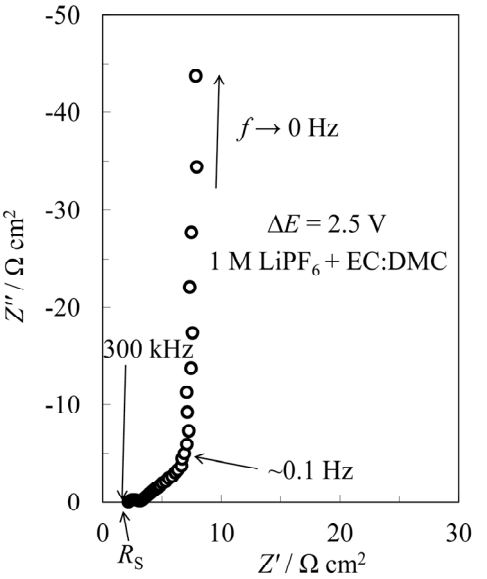

Figure 3. *Z*',*Z*''-plot of a SC test cell based on CDC electrodes in 1 M solution of $LiPF_6$ in a mixture of EC and DMC (1:1).

The ac frequency dependent series capacitance C_s of a SC device can be calculated from Z'' according to [7]:

$$C_s = -\frac{1}{\omega Z''}. \tag{27}$$

C_s can be defined in a complex form $C_s = C' - jC''$ having a real part C' and an imaginary part C'':

$$C' = \frac{-Z''}{\omega |Z|^2}, \tag{28}$$

$$C'' = \frac{Z'}{\omega |Z|^2}. \tag{29}$$

The low-frequency value of C' is equal to the SC capacitance measured during the constant current charge/discharge and C'' describes the resistive losses in the system, i.e. energy dissipation [1, 7, 116].

4.5.2.1. Complex power, energy and power density calculations

The rate of energy accumulation and release in different SCs can be compared on the basis of calculated characteristic time constants τ_R, which value shows how much time it takes to release half of the maximal stored energy [1, 7]. According to EIS data, τ_R can be calculated from the so-called relaxation frequency f_R, according to:

$$\tau_R = \frac{1}{2\pi f_R}. \tag{30}$$

The f-dependency plots for C'' go through a maximum at f_R, defining the τ_R. A more explicit presentation of this time constant is given through the definition of complex power of the SC device [7]. The values of complex power $S(\omega)$ can be expressed as:

$$S(\omega) = P(\omega) + jQ(\omega), \tag{31}$$

where the real part of power (active power) $P(\omega)$ is

$$P(\omega) = \omega C'' \left| \Delta V_{rms} \right|^2 \tag{32}$$

and the imaginary part of power (reactive power) $Q(\omega)$ is

$$Q(\omega) = -\omega C' \left|\Delta V_{\text{rms}}\right|^2 \tag{33}$$

with $\left|\Delta V_{\text{rms}}\right|^2 = \Delta V_{\text{max}} / \sqrt{2}$ (V_{max} is the maximal amplitude of ac voltage, 5 mV in this study). The ideal capacitor, i.e. a system with ideal capacitive behavior, has no real part of complex power as there is only the reactive contribution to the complex power, and a system with ideal resistive behavior has no imaginary part as this component only dissipates energy. SCs behave like a resistance–capacitance transmission line circuit (*RC*) balancing between the two states: resistive at $f \rightarrow \infty$ and capacitive at $f \rightarrow 0$. τ_{R} can be calculated from the frequency of interception point of the dependencies of normalized real part ($|P|/|S|$) and imaginary part ($|Q|/|S|$) of power on ac frequency.

For a more comprehensive comparison of different SCs, the maximum energy density (E_{max}, Wh kg^{-1}) and power density (P_{max}, kW kg^{-1}) can be calculated according to Equations (34) and (35) [7, 11, 12]:

$$E_{\text{max}} = \frac{C_{\text{s}}\, S_{\text{el}}\, \Delta E^2}{2\, m_{\text{el}}\, 3.6}, \tag{34}$$

$$P_{\text{max}} = \frac{\Delta E^2\, S_{\text{el}}}{4\, R_{\text{s}}\, m_{\text{el}}}, \tag{35}$$

where S_{el} = 2 cm^2. The low-frequency ($f = 1 \cdot 10^{-3}$ Hz) value for C_{s} (F cm^{-2}) is used, where the system has nearly ideal capacitive behavior, and the high-frequency ($f = 3 \cdot 10^5$ Hz) series resistance R_{s} (Ω cm^2), corresponding to the series *RC* circuit (3.6 comes from conversion of time and mass units). Only at middle ac frequencies the equivalent circuit gets a more complex form where, in addition to the high-frequency series elements, parallel *RC* circuit elements are important, taking into account the slow adsorption and mass transfer processes [7, 13].

4.5.2.2. Equivalent circuit for fitting of experimental data

Different models and approaches were considered and tested for the fitting of experimental impedance data, e.g. one developed by Levi and Aurbach for LIB multilayered porous composite electrodes [121] and a transmission line model for EDLCs by Itagaki et al [122]. The best mathematical fitting was obtained by using equivalent circuits worked out by Meyers et al [123] (Figure 4), developed to describe the impedance response of a porous electrode composed

of spherical intercalation particles. The carbons used as electrode materials are practically amorphous with a graphitization degree of a few per cent, so it is believed that Li- or Na-ion (maybe also Cs-ion) intercalation occurs in a small degree. Also there is probably SEI formation, depending on the electrolyte salt chemical composition. The equivalent circuit used takes these processes into account and describes well the systems under study [97, 98].

The Meyers model fits the experimental impedance data up to 0.05 Hz, therefore it has been slightly modified by replacing a constant phase element CPE_2 into the low frequency sub-circuit to take into account the low frequency adsorption processes at/into microporous non-homogeneous electrode surface (Figure 4b). Case (b) is the most general approximation that includes both internal and external interfacial impedance as well as a resistive film (SEI) formation. R_1 is the high frequency series resistance of the test system. The values of resistive film capacitance C_{film} and resistance R_{film} are determined by the SEI formation and/or by the pseudometallic characteristics of carbon materials, i.e. by the potential drop in the thin surface layer of carbon (in the so-called space charge region) and/or solvent monolayer [124–126]. However, these processes are inseparable from each other under the conditions applied in this work. R_{ct1} and C_{dl1} are the external resistance and double layer capacitance. R_{ct2} and CPE_2 are the internal charge transfer resistance and constant phase element, respectively, and Z_w is the Warburg-like diffusion impedance.

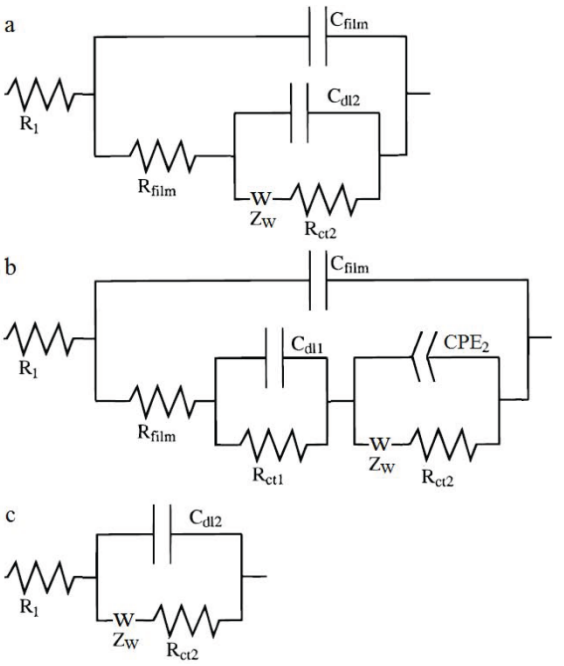

Figure 4. Equivalent circuits used for fitting of EIS data (explanations given in text) [123].

Low-frequency constant phase element impedance Z_{CPE} is expressed as:

$$Z_{CPE} = A^{-1}(j\omega)^{-\alpha_{CPE}}, \tag{36}$$

where A is the CPE coefficient and α_{CPE} is the CPE fractional exponent (if $\alpha_{CPE} = 1.0$, then A = capacitance).

Diffusion impedance Z_W is given as:

$$Z_W = \sigma_{ads}\ (j\omega)^{-\alpha_W}, \tag{37}$$

where σ_{ads} is the Warburg constant [115, 127] and α_W is the fractional exponent. The classical semi-infinite diffusion model applies when $\alpha_W = 0.5$, but often micro-meso-porous electrode based systems have α_W values slightly different from 0.5, indicating deviation toward finite-length Warburg model with adsorption boundary condition [128–130].

Case (a) in Figure 4 neglects R_{ct1} and C_{dl1}, and if there is no insulating film at electrode surface, then circuit (b) simplifies to case (c), not applicable to the electrode/electrolyte interfaces under study within the full extent of the potential region applied.

The low frequency intercalation capacitance (also called differential intercalation capacitance [121–123] or chemical capacitance [131]) for ion intercalating systems, redox electrodes (materials) and electronically conducting polymers is physically different from that of the micro-meso-porous EDL electrodes [116]. For ion intercalating electrodes the bulk capacitance is considered, but for the EDL electrodes we deal with a typical interfacial capacitance although distributed along the entire micro-meso-porous carbon structure. The shape of Nyquist plots (Z'',Z'-plots) is quite similar for these types of charge accumulation materials in the frequency region under study, but not identical. The frequency response for the ion intercalating electrode is expressed by the finite-space Warburg element, approaching the classical semi-infinite Warburg element [58, 116], at high ac frequencies, and frequency-independent capacitance at low frequency $f \rightarrow 0$. In case of ideally polarizable porous carbon electrodes there should be a mixture of the blocking electrode with specific diffusion impedance in the high-to-low frequency domain (accounting for the non-uniform distribution of current due to the hierarchical porous structure [122]) and a kind of electrode behavior characterized by the Melik-Gaykazyan and Frumkin model if specific adsorption is implied [132, 133]. In principle, equivalent circuit (b) in Figure 4 could be simplified for an ideally polarizable EDLC electrode so that low frequency capacitance would be described only by Z_w. However, the results of fitting show that CPE_2 in the circuit is inevitable to have good fitting of impedance spectra. This effect can be explained by the parallel occurrence of cation intercalation process, slow faradaic processes at microporous surface, and EDL formation with partial charge transfer step.

The comparison of experimental and theoretical Nyquist plots shows that, at the time being, the sensitivity of different methods and models is still too low to well separate the role of the main processes mentioned. Even at f = 0.001 Hz there is no so-called ideal limiting capacitive behavior for the materials under discussion due to the minor faradaic processes probably accompanying the intercalation and/or specific adsorption processes. In addition, it should be noted that the porous C(TiC) and C(Mo_2C) electrodes are inhomogeneous in thickness (Figure 6) and the model developed by Levi and Aurbach [121] is probably valid. Assuming the Li-ion (or Na-ion, Cs-ion) intercalation into carbon particles, the pores of larger particles are somewhat less accessible than these of the smaller particles. Thus, at moderate applied ac frequency one can establish limiting low-frequency capacitive behavior in the smaller particles, but for the larger particles a mixed process takes place, still close to the semi-infinite Warburg diffusion behavior. Due to the hierarchical porous structure of electrodes, the ion conductivity in micro-, meso- and macropores is probably different, caused by the adsorption/absorption of ions at microporous surface (decrease in concentration of charge carriers) at higher surface charge densities [59].

4.5.3. Constant current charge/discharge

Constant current charge/discharge (CCCD) is a current step method, where a constant current I is applied and the potential response $\Delta E(t)$ of the system under study is registered [2, 3, 12]. For a pure capacitor, the quantity of charge q of CCCD process is:

$$q = C\Delta E(t) = \int_0^t Idt \,. \tag{38}$$

For a circuit of resistance and capacitance in series, similar relation applies as in Equation (23), so considering Ohm's law and Equation (38), the CCCD potential response of an RC circuit is:

$$\Delta E(t) = IR + \frac{I\Delta t}{C} = I(R + \frac{\Delta t}{C}) \,, \tag{39}$$

where IR is the potential drop on CCCD (Figure 5). In such calculations, an exact capacitance value C_{CCCD} can be calculated from the slope of CCCD curves only when a linear function between t and $\Delta E(t)$ appears, according to:

$$C_{CCCD} = \frac{I\Delta t}{\Delta E(t)} \,. \tag{40}$$

In case of non-linear relation, integration method should be used to evaluate capacitance. CCCD method is often used for the cycle life analysis of different SC test systems.

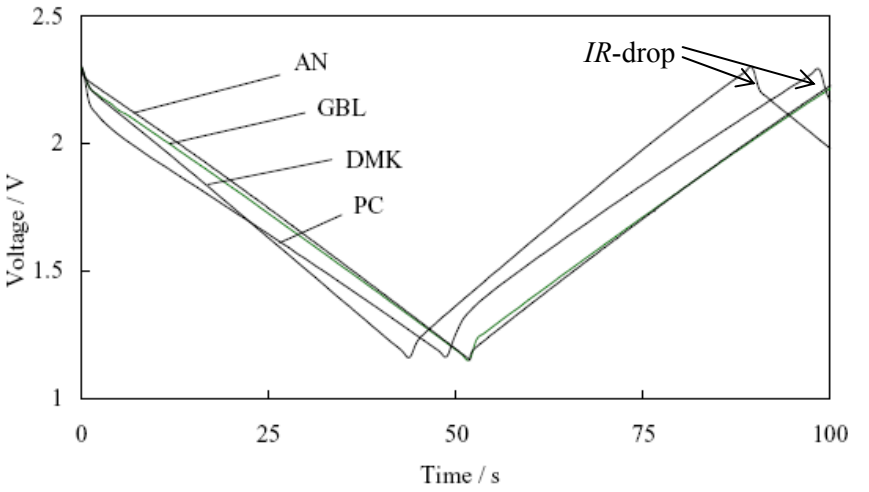

Figure 5. Constant current charge/discharge cycle at I = 0.5A and T = 298K for SCs filled with different electrolytes, noted in figure. GBL – γ-BL, DMK – dimethyl ketone [12].

5. EXPERIMENTAL

5.1. Electrode materials and electrolytes

The studied electrodes were prepared from micro-meso-porous CDC powders, synthesized by the high-temperature chlorination method [65, 68] either from TiC (Alfa Aesar, 99.5%, metals basis, typically 2 μm powder) at 950 °C, or from Mo_2C (Sigma-Aldrich, ρ = 9.12 g cm^{-3}, –325 mesh powder) at 800 °C. These materials are further noted as C(TiC) and C(Mo_2C), respectively. Flexible ~105 ± 5 μm thick layers of the porous carbon electrodes with hierarchical structure were press-rolled from a mixture comprised of 95% active material and 5% polytetrafluoroethylene binder (60% solution in H_2O, Aldrich). The scanning electron microscopy (SEM) images of electrode layers show that the carbon particle size for both materials varies widely from 0.5 to 5 μm, and narrow binder filaments (white lines) connecting carbon particles can be seen at electrode surface (Figure 6). After drying at 120 °C under vacuum, one side of the carbon electrodes was covered with pure Al (99.999%) layer (2–3 μm) by magnetron sputtering method (AJA International) [134] for good electrical contact and to reduce the ohmic potential drop (*IR*-drop) during charge/ discharge process.

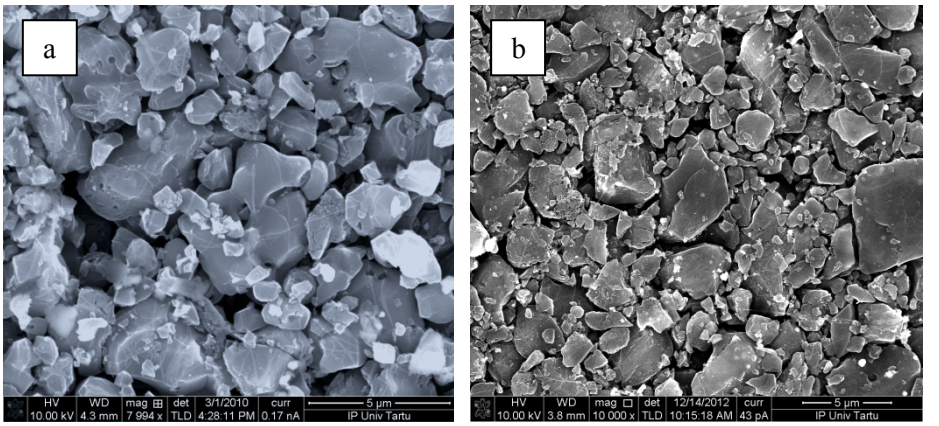

Figure 6. SEM images of (a) C(TiC) electrode; and (b) C(Mo_2C) electrode.

The structure of electrode materials was analyzed by Raman spectroscopy method. The spectra were recorded using a Renishaw inVia micro-Raman spectrometer applying Ar laser excitation (operating wavelength λ_L = 514 nm). The obtained Raman spectra are very similar for C(TiC) and C(Mo_2C) materials (Figure 7). The first-order Raman spectra indicate the mainly amorphous structure of the carbon materials under study, demonstrating two characteristic peaks – the so-called graphite (G) peak at ~1589 cm^{-1} and the so-called disorder-induced (D) peak at ~1348 cm^{-1} [67, 135, 136]. G-peak corresponds to

the in-plane bond stretching motion of pairs of C atoms in sp^2 configuration with E_{2g} symmetry and occurs at all sp^2 sites, not only for those atoms located in hexagonal graphene (graphite) structure. D-peak is a breathing mode with A_{1g} symmetry which is forbidden in perfect graphite and only becomes active in the presence of disorder in graphitic structure [136–138]. Raman spectra in Figure 7 also have second-order peaks D* and G* at ~2690 cm^{-1} and ~2930 cm^{-1}, more commonly noted together as 2D peak, which is related to the three-dimensional ordering of the graphitic structure [136, 138]. Thus, C(TiC) and C(Mo_2C) carbons are partly graphitized.

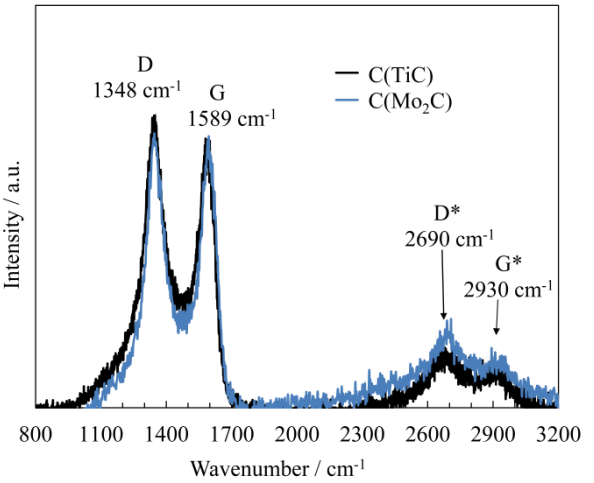

Figure 7. Raman spectra for C(TiC) and C(Mo_2C) carbons.

The porous structure of the CDC powders was studied by nitrogen adsorption at 77 K using the Nova 1200e system (Quantachrome, USA) or ASAP 2020 system (Micromeritics, USA). The adsorption isotherms were analyzed by the BET, *t*-plot and NLDFT models. The porosity characteristics and pore size distributions, presented in Table II and Figure 8, indicate that the studied carbons have very similar specific surface areas around 1690 $m^2\ g^{-1}$, but the volume of pores is somewhat higher for C(Mo_2C). Both C(TiC) and C(Mo_2C) carbons are mainly microporous with some mesoporosity (Table II). The NLDFT pore size distribution maximum (PSDM) for C(TiC) is located at 1.08 nm, and C(Mo_2C) has two PSDMs at 1.15 nm and at 3.80 nm, thus C(Mo_2C) has slightly wider micropores and larger amount of mesopores.

Table II. Porous structure characteristics of C(Mo_2C) and C(TiC) electrode materials.

Electrode material	S_{BET} / m^2 g^{-1}	S_m / m^2 g^{-1}	V_m / cm^3 g^{-1}	V_{tot} / cm^3 g^{-1}
C(TiC)	1698	1661	0.83	0.90
C(Mo_2C)	1675	1559	1.18	1.40

S_{BET} – specific surface area calculated by BET theory at P/P_0 = 0.05…0.2; S_m – micropore area from *t*-plot method; V_m – micropore volume from *t*-plot method; V_{tot} – total pore volume at P/P_0 = 0.999.

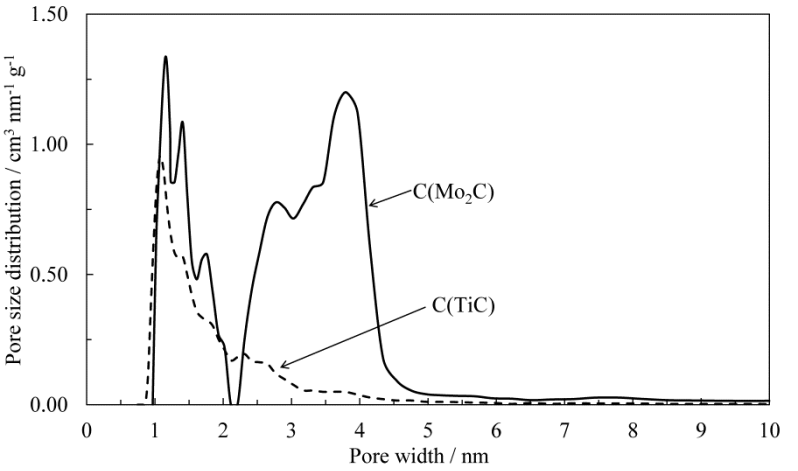

Figure 8. The pore size distribution for the C(Mo_2C) and C(TiC) electrode materials, calculated according to NLDFT.

Different alkali metal salt solutions were studied as supercapacitor electrolytes in a solvent mixture of very pure ethylene carbonate (EC, Selectipur®, Merck) and dimethyl carbonate (DMC, > 99%, H_2O < 0.002%, Sigma-Aldrich) (1:1 by volume). 1 M solutions were prepared from lithium perchlorate ($LiClO_4$, 99.99%, Aldrich), lithium hexafluorophosphate ($LiPF_6$, 99.99%, battery grade, Aldrich), lithium trifluoromethanesulfonate ($LiCF_3SO_3$, 99.995%, Aldrich), lithium bis(oxalato)borate ($LiB(C_2O_4)_2$, Chemetall, standard battery grade), sodium hexafluorophosphate ($NaPF_6$, 98%, Aldrich) or sodium perchlorate ($NaClO_4$, ACS reagent, ≥98%, Sigma-Aldrich). Also, 0.8 M solution of cesium carborane ($CsCB_{11}H_{12}$, Strem Chemicals) was tested in the same solvent mixture.

The specific conductivity κ of electrolyte solutions was determined using a self-made conductivity measurement test cell with two platinum plate electrodes. The test cell was filled with electrolyte solution and the high-frequency (f > 10 kHz) series resistance was measured at ΔE = 0.0 V by EIS method. 0.01 M and 0.1 M KCl solutions were used as calibration references to determine the conductivity constant of the cell. The calculated κ values for the

electrolytes under study are presented in Table III, except for 0.8 M $CsCB_{11}H_{12}$ in EC:DMC. The highest conductivity was measured for $NaPF_6$, followed by $LiPF_6$, explained by the higher solvation number (and higher solvation energy) for the smaller Li^+ ions [139]. Same explanation applied for the small difference in $NaClO_4$ and $LiClO_4$ based electrolytes. The decrease in electrolyte conductivity when changing salt anion from PF_6^- to ClO_4^- (with bare anion dimensions of 54 $Å^3$ and 47 $Å^3$ [140], respectively) is explained by the PF_6^- anion weaker coordinating ability compared to ClO_4^- anion and higher degree of ion-pairing in ClO_4^- electrolytes [141–143].

Table III. Specific conductivities of 1 M alkali metal salt solutions in EC:DMC (1:1) solvent mixture at $T = 22$ °C.

Electrolyte salt	$LiPF_6$	$LiClO_4$	$LiB(C_2O_4)_2$	$LiCF_3SO_3$	$NaPF_6$	$NaClO_4$
κ / mS cm^{-1}	10.54	9.15	5.85	3.01	12.29	9.18

5.2. Electrochemical measurements

Electrochemical measurements were done in special hermetic HS two-electrode and HS-3E three-electrode aluminium test cells (TCs) (Hohsen Corp., Japan) that were assembled in a glove-box Labmaster sp (MBraun, Germany) at 22 ± 1 °C in argon atmosphere at clean and dry conditions (99.9999%, AGA; $O_2 < 0.1$ ppm, $H_2O < 0.1$ ppm). The working electrode (WE) and counter electrode (CE) in three-electrode systems were cut from the same electrode active layer with the electrode cross-sectional surface area being much smaller for WE (0.2827 cm^2) compared to CE (2.0 cm^2) in order to ensure much higher effective surface area for CE, i.e. higher electrode capacitance. In the two-electrode TCs both electrodes were 2.0 cm^2. The reference electrode (RE), used for Li- and Na-salt electrolyte based TCs, was Li-ring (Li/Li^+, approximately –3.0 V vs. standard hydrogen electrode SHE) in the same electrolyte solution. Negligible amount of respective Li-salts were added to the Na-salt based electrolytes for the establishment of stable RE potential. Ag/AgCl RE (~0.2 V vs. SHE) was used in case of $CsCB_{11}H_{12}$ electrolyte based TCs. Mesoporous ~25 μm thick polypropylene separators (Celgard® 2400) were used that have good wetting and ion-conduction compatibility with the carbonate solvents based electrolyte [114]. Assembled TCs were impregnated with the working electrolyte solution for 24 h before electrochemical measurements. Three-electrode and two-electrode TCs will be hereafter noted as 'salt'-3TC and 'salt'-2TC, respectively. The C(TiC) electrodes were used in TCs with $LiPF_6$, $LiClO_4$, $LiCF_3SO_3$, and C(Mo_2C) electrodes were tested in $LiB(C_2O_4)_2$, $NaClO_4$, $NaPF_6$, and $CsCB_{11}H_{12}$.

The electrochemical characteristics of the different assembled TCs were studied using cyclic voltammetry, electrochemical impedance spectroscopy and constant current charge/discharge methods. Impedance spectra were recorded using a 1252A Solartron frequency response analyzer and a SI1287 potentiostat with a 5 mV modulation. The non-linear least squares method was applied to fit theoretically calculated impedance plots to the experimental ones, using ZView program versions 2.8d and 3.2c [127].

6. RESULTS AND DISCUSSION

6.1. Cyclic voltammetry measurements

CVs were measured both for three- and two-electrode TCs at fixed ν from 0.5 to 100 mV s^{-1} to establish the region of ideal polarizability. Three-electrode measurements give information about the anodic and cathodic electrochemical stability limits of the studied electrode/electrolyte interface, adsorption processes and possible faradaic reactions. C_{WE} vs. WE potential E (vs. Li/Li^+) curves for Li-salts and Na-salts based TCs are presented in Figures 9 and 10, with the maximum E region being 0.5 to 5.0 V for Li-salts-3TCs and 1.0 to 4.8 V for Na-salts-3TCs [95, 97, 98, 105]. All electrolyte/electrode interfaces, except $CsCB_{11}H_{12}$-3TC, exhibit nearly mirror image symmetry of the current responses in reference to the zero current line at moderate ν from 5 to 50 mV s^{-1} in the region $1.0 < E < 4.5$ V, i.e. the region of ideal polarizability, and are nearly independent of the number of current cycles n (if $3 < n \leq 100$).

A more complicated shape of C_{WE},E-curves has been established at lower potential scan rates $\nu \leq 1$ mV s^{-1} (Figures 9 and 10). The slow mixed kinetic anions adsorption process with partial charge transfer starts at $E \sim 3.5$ V on the anodic scan, and oxidation processes at more positively charged electrode surface ($E > 4.3$ V). The highest capacitance was calculated at $E > 4.3$ V for $LiB(C_2O_4)_2$-3TC and $LiClO_4$-3TC [97, 98] (Figure 9). The quick exponential increase in current density for $LiClO_4$-3TC at $E > 4.8$ V in Figure 9 indicates oxidative decomposition of the electrolyte. The same effect was observed for Na-salts-3TCs, which is why the potential scan was reversed at $E = 4.8$ V in Figure 10 [105]. In case of $LiPF_6$-3TC no remarkable oxidation processes were observed (Figure 9). Corresponding reduction processes and desorption of anions take place at $E \leq 2.5$ V.

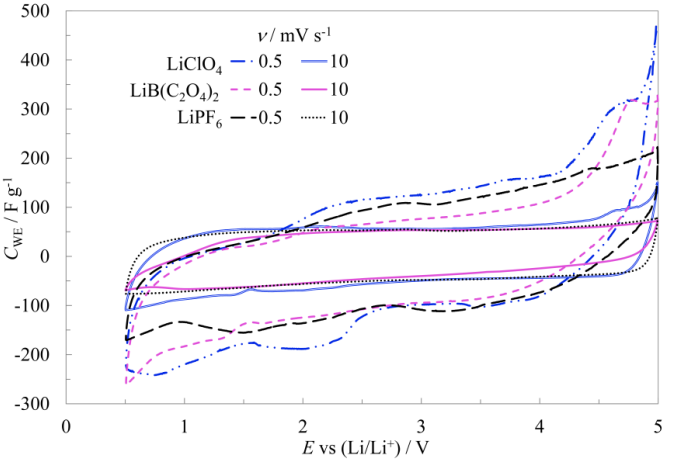

Figure 9. Current density of different Li-salt based 3-electrode systems, expressed as gravimetric capacitance vs. WE potential at 0.5 and 10 mV s^{-1}.

At negative potential scan direction (E < 1.0 V), i.e. reduction curve, the formation of SEI takes place [19, 21, 59, 97, 98, 105, 144]. The increase in capacitance during SEI formation is probably caused by the decrease in thickness of SEI or the increase in dielectric permittivity of the surface film. For Na-salts-3TCs the current density increase was remarkable at E < 1.0 V (not shown in Figure 10). This might be due to the differences in Li^+ and Na^+ solvation energies and also related to the SEI formation kinetics at the electrode surface at E < 1.0 V. During the reverse potential scan from 0.5 V to more positive E in case of Li-salts-3TCs, the surface processes are very slow and blocked due to SEI, and thus low capacitance values have been obtained (Figure 9). Only at E > 2.5 V the oxidation of SEI-forming components seems to occur. The blocking effect of SEI seems to be the strongest for $LiB(C_2O_4)_2$-3TC. Such strong blocking effect is not seen in Figure 10 for the Na-salts-3TCs due to the higher switchover potential of 1.0 V, but in reality a film formation occurs also for these systems under study.

Inside the region of ideal polarizability, the C_{WE} values for PF_6^- and ClO_4^- anion containing electrolytes are rather similar. Only at low ν, slightly higher capacitance values have been calculated for the $NaPF_6$-3TC compared to other salts. The lowest gravimetric capacitance values in the wide potential region studied were obtained for $LiB(C_2O_4)_2$-3TC, except near the switchover potentials (Figures 9 and 10). It should be noted that the electrochemical stability of Al current collector needs additional studies at E > 4.5 V and E < 0.7 V (vs. Li/Li^+), where remarkable faradic processes have been observed.

As can be seen from Figure 9 for the Li-salts-3TCs, the cathodic cut-off potential (0.5 V) is by at least 0.5 V larger in relation to the point of zero charge potential (~3.0 V) than the corresponding anodic cut-off potential of 5.0 V. In addition to trivial effect of enlargement of the anodic current in the vicinity of the anodic cut-off potential due to oxidation of the intermediate species formed by reduction of electrolyte species close to the cathodic cut-off potential, there may exist a specific effect of trapping of cations in microporous carbons at excessively negatively charged carbon electrode surface [145]. Cations trapped in carbon micropores at extremely high electrode charge density cannot be desorbed in the native potential domain of the negatively charge carbon electrode, in other words partially irreversible adsorption/desorption occurs on the microporous surface of the studied electrodes.

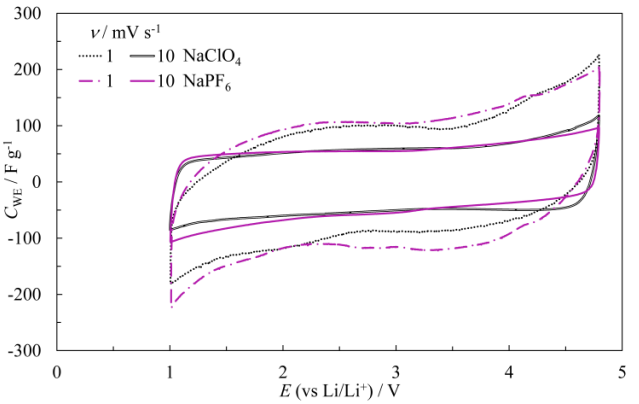

Figure 10. Current density of different Na-salt based 3-electrode systems, expressed as gravimetric capacitance vs. WE potential at 1 and 10 mV s^{-1}.

Different behavior from the studied Li- and Na-salts was observed in case of $CsCB_{11}H_{12}$-3TC (Figure 11). The oxidation of $CB_{11}H_{12}^-$ anions was remarkable already at WE potentials $E > 4.2$ V (the RE used for measurements was Ag/AgCl, but the potential scale is recalculated to Li/Li^+ for better comparison). On the cathodic scan direction, exponential increase in current density occurred at $E < 1.1$ V during the first CVs measured and an interesting peak occurred on the reverse potential scan. It is assumed that this peak is related to the specific and partly irreversible Cs^+ adsorption (or intercalation) at the micro-meso-porous carbon surface. However, from the 7th scan the CVs have a consistent shape, where there is no exponential current increase around $E \sim 1.1$ V. Thus, the porous carbon surface is probably being slightly modified through the specific adsorption and/or electrolyte reduction during the first scans, but there is no extensive blocking effect as the calculated C_{WE} remains constant in the wider potential region (Figure 11).

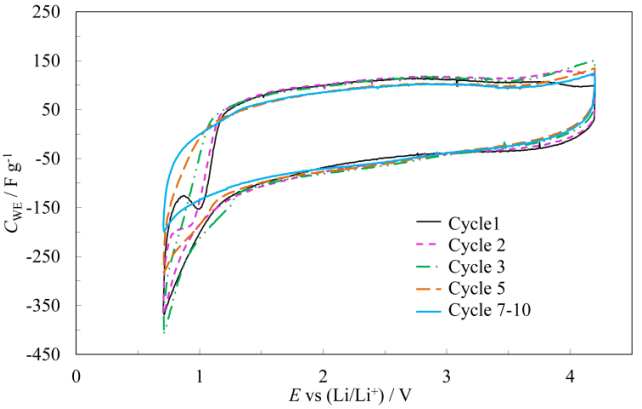

Figure 11. Gravimetric capacitance vs. WE potential during 10 first voltammetry cycles for $CsCB_{11}H_{12}$-3TC at $\nu = 1$ mV s^{-1}.

CVs were measured also for two-electrode TCs to characterize the electrode/electrolyte combinations in a working SC device. The CVs measured for $LiPF_6$-2TC, presented in Figure 12, have nearly rectangular shape up to $\Delta E < 3.2$ V and at $\nu \leq 100$ mV s^{-1}. Figure 13 demonstrates that the values of calculated gravimetric capacitance C_g per one electrode for the $LiPF_6$-2TC are nearly independent of ν when $\nu \leq 100$ mV s^{-1}, and thus nearly equilibrium values of C_g can be obtained. The observed sharp increase in C_g at $\Delta E > 3.0$ V is caused by the electroreduction of residual H_2O and O_2 traces at negatively charged electrode and oxidation of surface functionalities at positively charged electrode, respectively, as well as electrolyte salt (or solvent) decomposition. The loop, i.e. current delay on switching scan direction, in CVs at $\Delta E \geq 3.0$ V and at $\nu > 50$ mV s^{-1} is caused by the contact resistance between the micro-meso-porous carbon electrode and vacuum deposited Al-layer, and also by the high-frequency series resistance and capacitance of electrolyte inside the porous structure of carbon, as well as mesoporous separator material resistance [2, 3, 5, 7, 12, 13, 57].

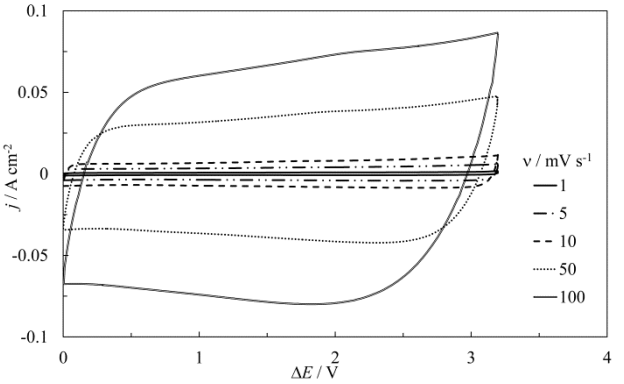

Figure 12. CVs for $LiPF_6$-2TC measured up to 3.2 V at different potential scan rates.

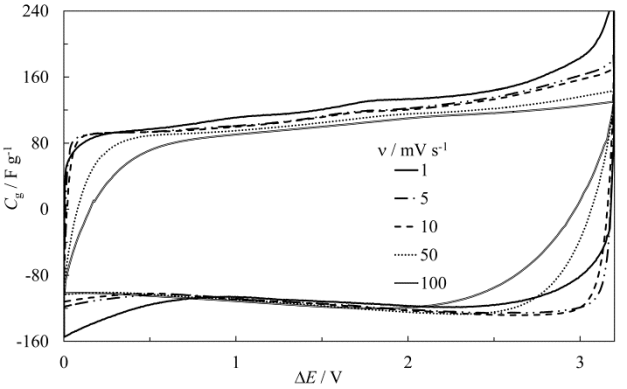

Figure 13. CVs presented as gravimetric capacitance C_g vs. ΔE for $LiPF_6$-2TC measured at different potential scan rates.

The CV analysis was made similarly for all TCs under study, from where the highest ΔE with nearly ideal capacitive behavior was determined, and approximate information about the resistance of the TCs based on different electrolytes was obtained from the ν–dependencies. The electrochemical behavior of different TCs is compared in Figure 14 [95–98, 105]. The highest ΔE can be applied in $NaPF_6$-2TC, being 3.4 V. As discussed earlier, $LiPF_6$-2TC shows nearly ideal capacitive behavior at $\Delta E \leq 3.2$ V, which is the same for $NaClO_4$-2TC. Faradaic decomposition of the electrolyte in $LiClO_4$-2TC starts to take place already at $\Delta E > 2.7$ V, being 0.5 V less than in case of $NaClO_4$-2TC. During cycling at $\Delta E > 2.7$ V quick and noticeable decrease in electrode capacitance due to surface blocking effect takes place (Figure 15), later affirmed also by impedance data. Also $LiB(C_2O_4)_2$-2TC can be used only up to $\Delta E = 2.7$ V and $CsCB_{11}H_{12}$-2TC up to $\Delta E = 3.0$ V without remarkable faradaic processes. In case of $LiCF_3SO_3$-2TC decomposition of electrolyte salt takes place already at low applied ΔE (later proved also by the EIS data for this system) and the decomposition products block the carbon electrode surface, indicated by the much smaller calculated C_g.

It can be seen from Figure 14 that, for the electrochemically stable electrolyte systems at ΔE in the region of ideal polarizability, the capacitance of the SCs is rather determined by the electrode materials than by the electrolyte solutions used. Even though the amount of mesopores is somewhat different for C(TiC) and C(Mo_2C) electrode materials, the S_{BET} ~1690 m^2 g^{-1} and S_m ~1600 m^2 g^{-1} are rather similar for the two materials (Table II), and surprisingly similar limiting C_g values were calculated for the TCs under study, being in the range of ~110 to 130 F g^{-1} (determined from discharge curves in the region $2.5 < \Delta E < 3.2$ V). The smallest C_g values were calculated for $CsCB_{11}H_{12}$-2TC that has the largest anions in the composition and slightly lower salt concentration (0.8 M), and where probably Cs^+ specific adsorption occurs with partial blocking of ion diffusion paths. In the lower ΔE region from 0.0 to 1.0 V, the highest discharge C_g was obtained for $NaPF_6$-2TC and $LiPF_6$-2TC, first one with C(Mo_2C) and second with C(TiC) electrodes. The effect of electrode microstructure (micropore and mesopore ratio, etc.) and the effect of Na^+ or Li^+ in the salt composition (solvation/desolvation) are at this point inseparable. The C_g value decreased for both Na- and Li-salt at $\Delta E < 1.0$ V by changing the salt anion from PF_6^- to ClO_4^- that could be explained by the higher coordinating ability (and ion-pairing) of ClO_4^- anions compared to PF_6^- anions. Therefore, the electrostatic attraction forces at $\Delta E < 1.0$ V are insufficient for the partial solvation shell removal from ClO_4^-, causing reduced anion adsorption in the porous network of C(Mo_2C) and C(TiC) electrodes.

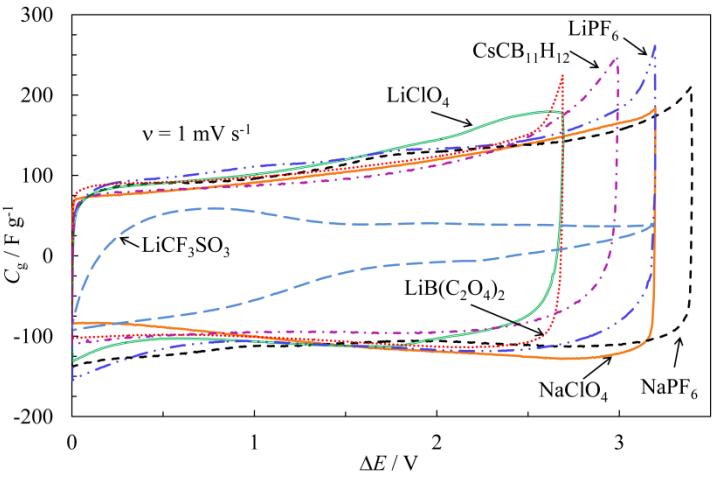

Figure 14. CVs presented as gravimetric capacitance C_g vs. ΔE for different two-electrode TCs under study, measured at $\nu = 1$ mV s^{-1}.

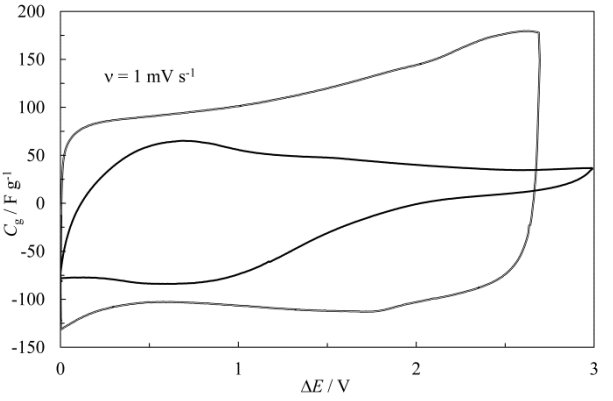

Figure 15. CVs presented as gravimetric capacitance C_g vs. ΔE for $LiClO_4$-2TC at $\nu = 1$ mV s^{-1}.

6.2. Analysis of impedance spectroscopy data

Nyquist plots were measured for both two- and three-electrode TCs at different applied potentials in ac frequency range from $1 \cdot 10^{-3}$ Hz to $3 \cdot 10^{5}$ Hz with a 5 mV modulation. The complex plane impedance plots of two-electrode TCs describe the overall response of a SC device on the applied av signal.

Experimental Nyquist plots for $NaClO_4$-2TC and $NaPF_6$-2TC are linear and practically vertical at low ac frequencies up to $\Delta E \leq 3.2$ V and $\Delta E \leq 3.4$ V, respectively, indicating nearly ideal capacitive behavior (Figure 16a) [105]. Only at higher applied ΔE the low-frequency parts of Z'',Z'-plots slightly start to incline due to similar faradaic processes already mentioned in the analysis of

CVs of $LiPF_6$-2TC (Figure 13). The phase angle θ absolute values are higher than 88° for the Na-salts TCs, thus approaching the ideal capacitive behavior ($\theta = -90°$). The R_s values are slightly higher for $NaClO_4$-2TC and depend more on the applied ΔE by increasing at higher ΔE = 3.2 V (Figure 16b).

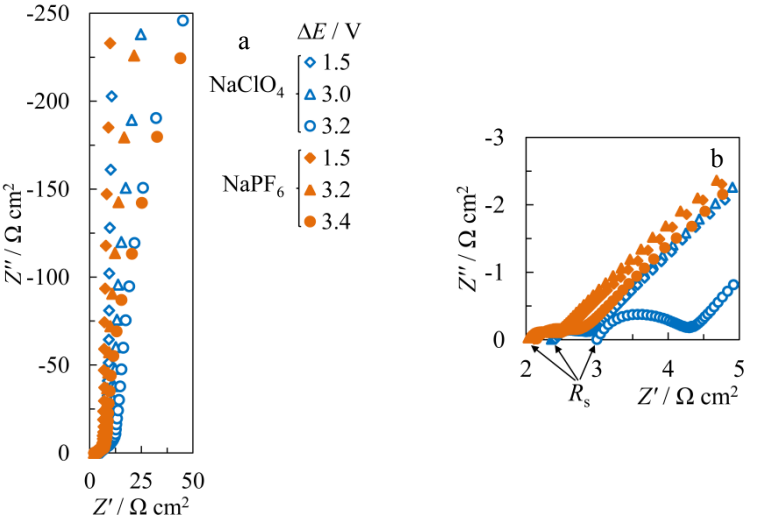

Figure 16. Comparison of Nyquist plots of $NaClO_4$-2TC and $NaPF_6$-2TC (a); and high-frequency inset of the plots (b) at different ΔE noted in the figure.

The Z'',Z'-plots of different TCs under study were compared at ΔE = 2.5 V in Figure 17 [95–98, 105]. The low-frequency parts of the plots indicate that nearly ideal capacitive behavior with vertical plots is established for all TCs except for $LiClO_4$-2TC and $LiCF_3SO_3$-2TC for which mixed kinetic processes occur at low ac f applied (Figure 17a). The length of the 'porous electrode section' for different electrolyte based TCs can be compared on the basis of Figure 17b. It can be seen that the 'knee' on the Z'',Z'-plots is located at the lowest f for PF_6^- anion based TCs and f increases in the order: $NaClO_4$-2TC < $LiB(C_2O_4)_2$-2TC < $CsCB_{11}H_{12}$-2TC, i.e. with the increase in solvated anion size. Somewhat longer –45° region for $NaClO_4$-2TC compared to $NaPF_6$-2TC could be explained by the PF_6^- coordinating ability, discussed earlier. $LiClO_4$-2TC and $LiCF_3SO_3$-2TC plots decline from –45° due to complex mixed kinetic processes. Also electrolyte salt cation influence on the frequency of reaching limiting adsorption behavior has been observed caused by the higher Li^+ solvation energy compared to Na^+, and probable specific adsorption of Cs^+ with the accompanying blocking of diffusion paths. Thus, the f decreases from Na^+ to Li^+ to Cs^+. Also the R_s values somewhat increase in the same order, from 2 to 3.4 Ω cm^2, which is in good correlation with the measured specific conductivities of the electrolytes (Table III). The higher R_s for $CsCB_{11}H_{12}$-2TC can be explained by the bulky anions in the electrolyte salt composition and also

by the slightly lower electrolyte concentration. However, for $LiClO_4$-2TC somewhat higher R_s is caused by the beginning of electrolyte decomposition at ΔE = 2.5 V, and for $LiCF_3SO_3$-2TC even much higher R_s was established due to surface blocking effects.

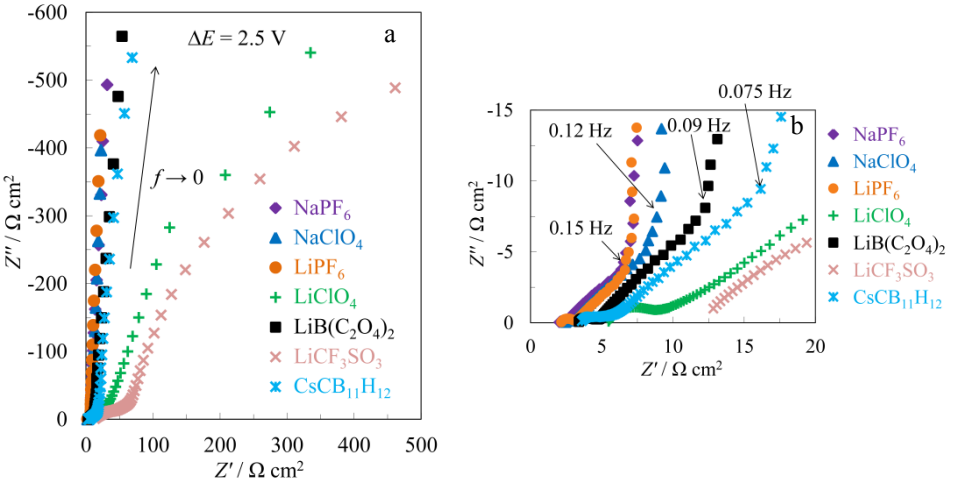

Figure 17. Comparison of Nyquist plots of different 2-electrode TCs under study (a); and magnification of the high-frequency region of the plots (b) at ΔE = 2.5 V.

The Nyquist plots for $LiCF_3SO_3$-2TC in Figure 18 indicate that the decomposition of $LiCF_3SO_3$ takes place already at ΔE = 0.0 V and complex faradaic processes, i.e. mixed kinetic behavior, occur at all studied cell potentials [96]. The R_s values are approximately an order of magnitude higher compared to the electrochemically stable electrolytes based TCs (Figure 17b) due to the blocking of the electrode surface by decomposition products, also observable from the CVs in Figure 14.

The C_s values, calculated from EIS data, scale up to a limiting value when $f \rightarrow$ 0. This capacitance plateau is characteristic to a system with ideal capacitive behavior [4, 12, 95–98, 105]. The limiting C_s values at different applied ΔE are given in Figure 19 for the different TCs under study. The general trend for TCs based on electrochemically stable electrolyte solutions is a slight increase in C_s at applied ΔE > 1.0 V, up to a TC-specific ΔE from where further extensive faradaic processes and/or specific adsorption start to take place with accompanying steep increase in C_s values. The linear increase in C_s with ΔE can be explained by the decrease in the effective area engaged by an adsorbed ion at the electrode surface of high charge density, decreasing the repulsion between similarly charged ions within the EDL region. Only for $LiClO_4$-2TC the C_s values noticeably decrease at $\Delta E \geq$ 2.5 V, and for $LiCF_3SO_3$-2TC already at ΔE > 0.0 V due to the electrolyte decomposition processes. The calculated C_s values coincide well with the calculated C_g from CV measurements (Figure 14),

from where also the slight increase in capacitance for the PF_6^- anion containing TCs at $\Delta E < 1.0$ V was established.

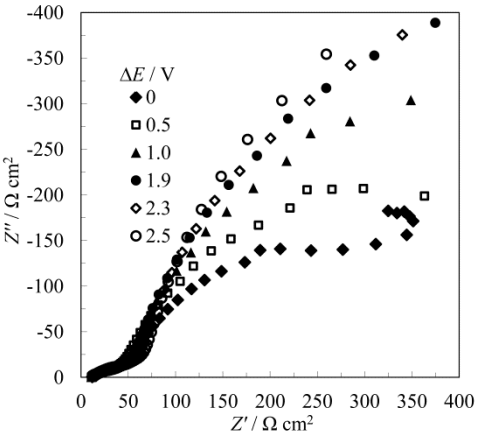

Figure 18. Comparison of Nyquist plots of $LiCF_3SO_3$-2TC at different ΔE, noted in the figure.

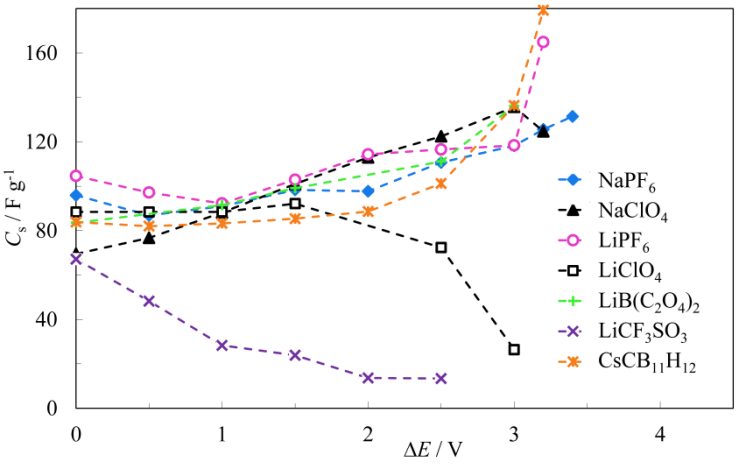

Figure 19. Dependence of low-frequency ($f = 1 \cdot 10^{-3}$ Hz) series capacitance on cell potential for different TCs under study.

Nyquist plots were also measured for the three-electrode systems and to the first approximation were fitted using equivalent circuits developed by Meyers et al [123] in order to describe separately the studied electrode/electrolyte interfaces at different applied potentials, i.e. the interface working as negatively charged or as positively charged electrode. The experimental Nyquist plots together with solid lines of fitting data for $NaPF_6$-3TC and $NaClO_4$-3TC are presented in Figure 20. Similar plots were obtained also for $LiPF_6$-3TC, $LiClO_4$-3TC and $LiB(C_2O_4)_2$-3TC [97, 98]. At applied WE potentials around the point of zero charge potential (~3.0 V vs. Li/Li^+), the Z'',Z'-plots have such shape as described earlier, where nearly ideal capacitive behavior is established at low f and semi-infinite diffusion-like process limitation occurs at moderate f.

At lower electrode potentials E < ~2.5 V, depending on the composition of the electrolyte used, systematic deviation from ideal capacitive behavior toward mixed kinetic mechanism occurs at f < 0.1 Hz with mass transfer limitation due to slow diffusion processes at/inside the porous electrode in addition to the slow adsorption step. Intercalation of Li^+ and Na^+ into the partially graphitized C(TiC) or C(Mo_2C) electrodes and the beginning of SEI formation are the rate determining processes at $E \leq 1.0$ V, where the high-frequency semi-circle is wider, indicating higher SEI resistance, and complex mixed kinetic processes take place at lower f. At higher WE potentials (E > ~4.0 V vs. Li/Li^+) adsorption of electrolyte anions with partial charge transfer occurs and the low-frequency behavior is no longer purely double-layer capacitive [95, 97, 98, 105]. The much wider semi-circle observed for $NaClO_4$-3TC at E = 4.8 V is related to the beginning of faradaic electrolyte oxidation process, together with the partial charge transfer taking place with anion adsorption process (Figure 20b).

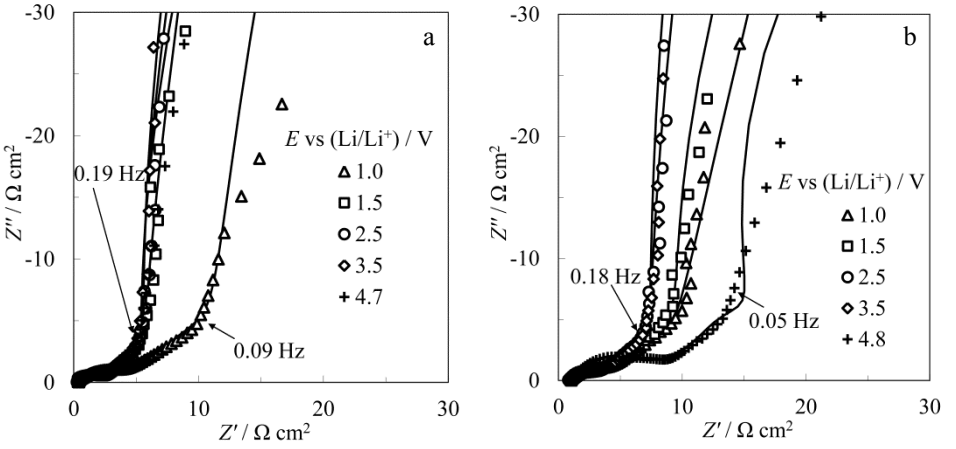

Figure 20. Nyquist plots at different WE potentials (points – experimental data, solid lines – fitting data from using equivalent circuit in Figure 4) for $NaPF_6$-3TC (a); and for $NaClO_4$-3TC (b).

The Nyquist plots for $CsCB_{11}H_{12}$-3TC do not have semi-infinite diffusion-like process limitation with –45° slope in the middle-frequency region, but complex mixed kinetic processes take place in the whole region of analyzed ac *f* (Figure 21). Also the semi-circle is much wider compared to other salts based TCs (Figure 20) [97, 98], indicating higher resistance of the external charge transfer and mass transport processes, which is affirmed by the fitting data, presented later. Nyquist plot at $E = 0.7$ V indicates that Cs^+ specific adsorption or intercalation process has high resistance and probably a highly resistive film forms on the negative electrode surface. Nearly ideal capacitive behavior can be seen at low *f* in the whole region of *E*.

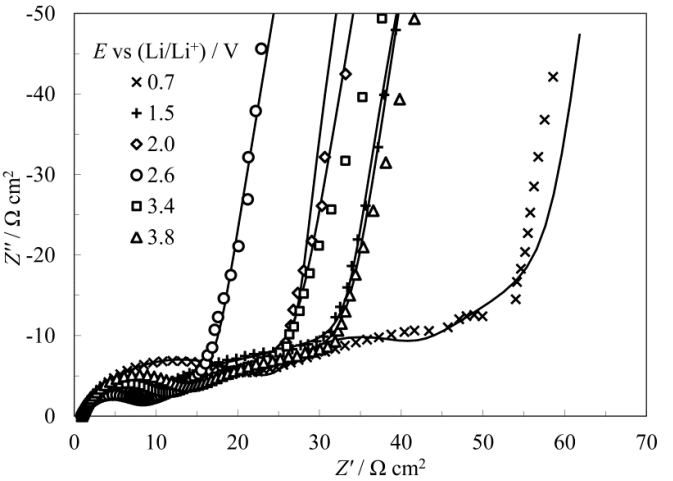

Figure 21. Nyquist plots at different WE potentials (points – experimental data, solid lines – fitting data from using equivalent circuit in Figure 4) for $CsCB_{11}H_{12}$-3TC.

6.2.1. Fitting of impedance data

Results of non-linear regression analysis [116, 118, 119, 123] (Figures 22–25) show that Nyquist plots for the tested TCs can be simulated using the equivalent circuit (b) given in Figure 4 with chi-square function $\chi^2 \geq 2\times10^{-4}$ and $\Delta^2 \geq 0.03$ [97, 98].

R_{film} values vary from nearly 0 to 1.8 Ω cm^2 for the TCs under study (Figure 22a). When comparing R_{film} of PF_6^- based TCs to those of ClO_4^- based TCs, the former have many times higher R_{film} in the wide *E* region, indicating a more compact resistive film on the electrode surface. Remarkable increase in R_{film} for $CsCB_{11}H_{12}$-3TC at $E < 2.5$ V could be related to the restricted diffusion of large specifically adsorbing Cs^+ ions through a formed surface film. Increase in R_{film} at $E \geq 3.0$ V for $LiB(C_2O_4)_2$-3TC is probably due to the big molar volume of asymmetric $B(C_2O_4)_2^-$ anions. Calculated C_{film} values are moderate ranging from $0.5\cdot10^{-5}$ to $1.3\cdot10^{-4}$ F cm^{-2} (Figure 22b) with a decrease in C_{film} at $E <$ ~1.0 V, where SEI formation takes place.

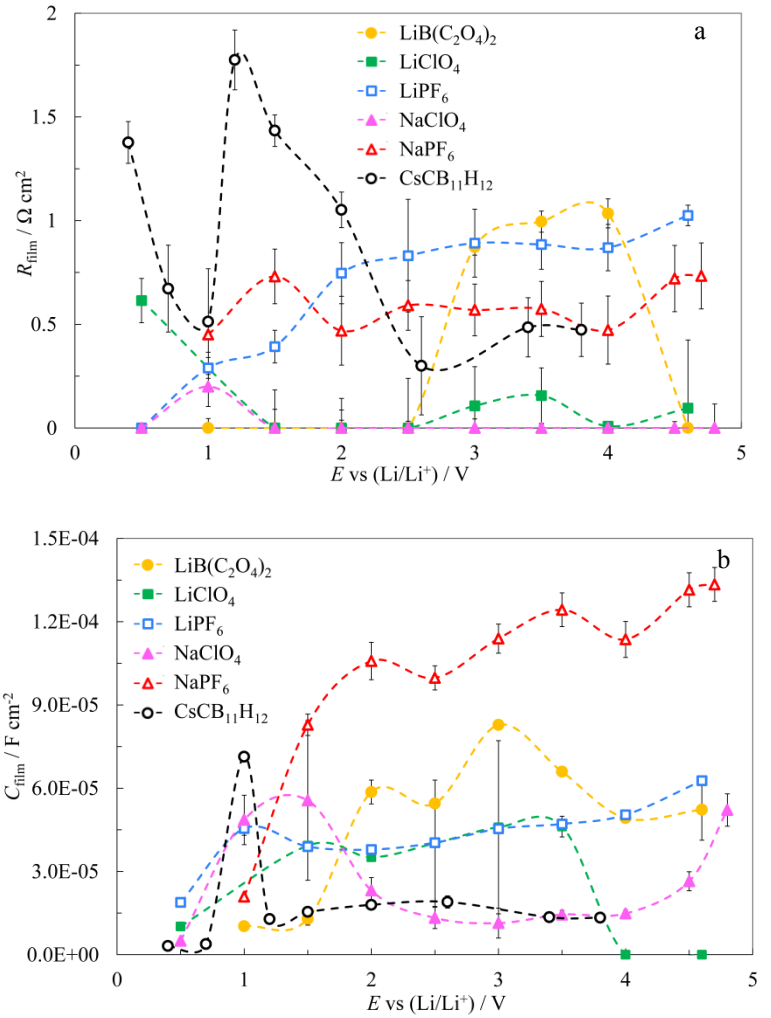

Figure 22. Resistive film resistance R_{film} (a); and capacitance C_{film} (b) vs. working electrode potential for different TCs, noted in the figure.

Moderate R_{ct1} values, comparable to R_{film} values and slightly smaller than R_{ct2}, were calculated (Figure 23a). Similarly to R_{film}, the R_{ct1} values increased at $E \geq 3.0$ V for $LiB(C_2O_4)_2$-3TC. The C_{dl1} values obtained are approximately an order of magnitude higher (in the range 10^{-3} F cm^{-2}) than the C_{film} values (in the range 10^{-5}…10^{-4} F cm^{-2}) for the respective TCs under study (Figure 23b).

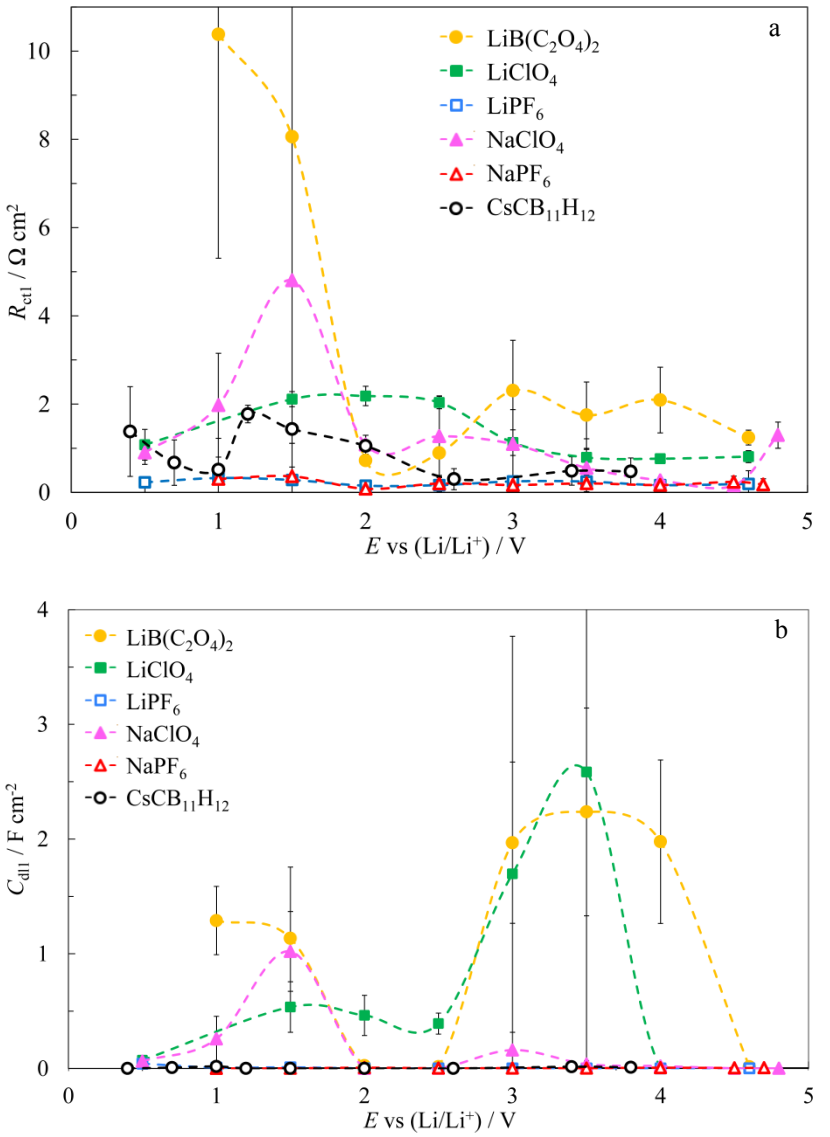

Figure 23. External charge transfer resistance R_{ct1} (a); and external double layer capacitance C_{dl1} (b) vs. working electrode potential for different TCs, noted in the figure.

The R_D values (Figure 24a) are noticeably higher than R_{film}, R_{ct1} and R_{ct2} values. The sequence of increase in R_D, when comparing different electrolyte based TCs, is in good correlation with the two-electrode 'porous electrode section' data (Figure 17b) at $E > 1.5$ V. At $E < 1.5$ V, the steep increase in R_D for $CsCB_{11}H_{12}$-3TC could be explained by the diffusion path blocking due to specific adsorption of large Cs^+ ions, and by the complex formation of SEI in

case of Li- and Na-salts, where R_D increase is observed for ClO_4^- and $B(C_2O_4)_2^-$ anions based TCs, referring again to the SEI dependence on the salt anion. The α_w values (Figure 24b) are around 0.5 in the region 2.0 V < E < 4.0 V, approaching to the classical semi-infinite diffusion model (α_w = 0.5). At the anodic and cathodic potential limits, α_w change indicates deviation of the tested systems from the semi-infinite Warburg diffusion model toward finite-length Warburg model with adsorption boundary condition [128–130].

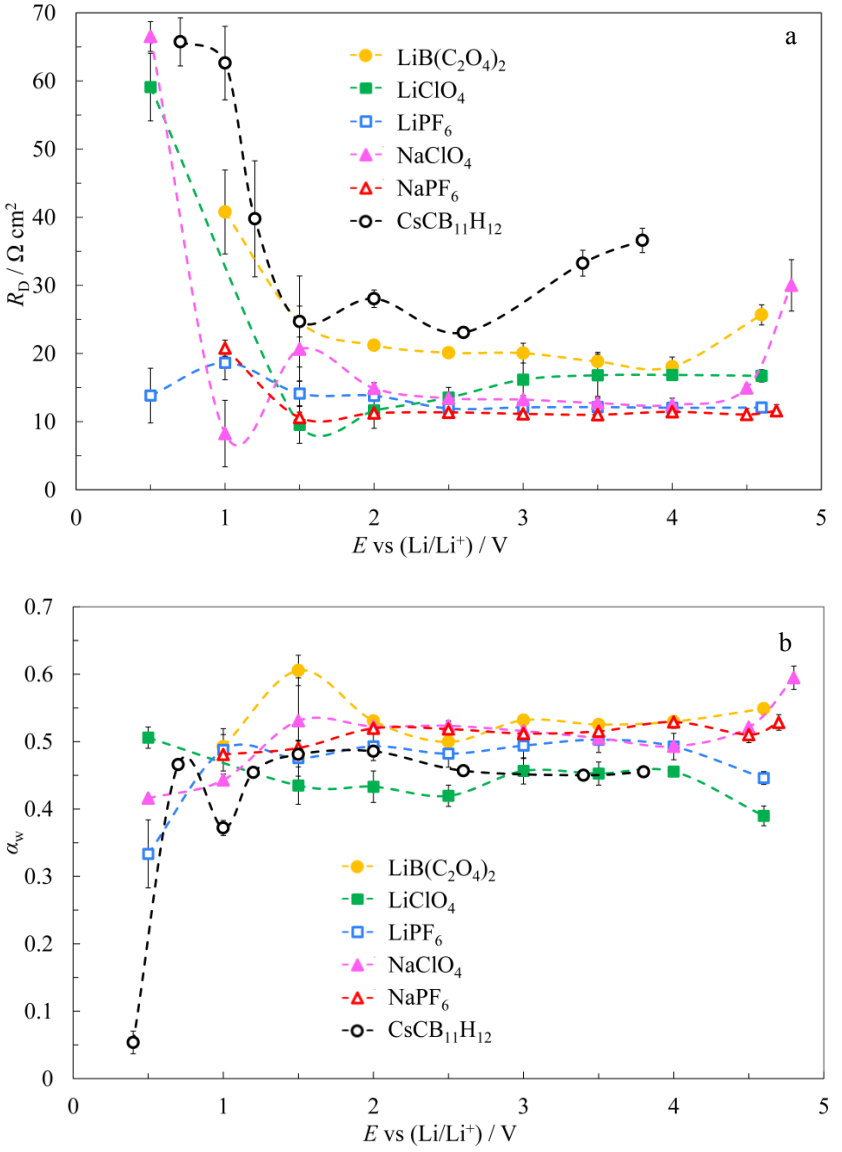

Figure 24. Diffusion resistance R_D (a); and Warburg fractional exponent α_W (b) vs. working electrode potential for different TCs, noted in the figure.

R_{ct2} values (Figure 25) are maximal for the $CsCB_{11}H_{12}$-3TC containing the bulky anions and cations, especially in the region, where the specific adsorption of Cs^+ should start (E ~ 1.0 V). The lowest R_{ct2} was established for TCs with PF_6^- based electrolytes.

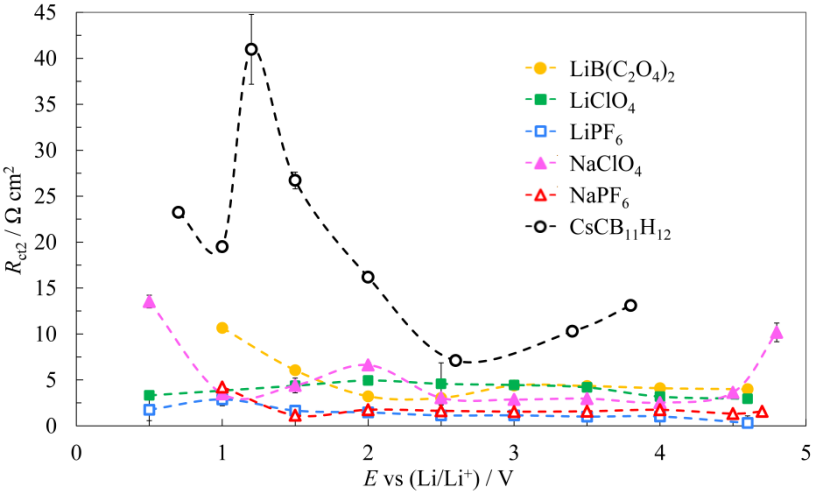

Figure 25. Internal charge transfer resistance R_{ct2} vs. working electrode potential for different TCs, noted in the figure.

6.2.2. Time constants, energy and power densities

A comparison of complex power plots, presented at ΔE = 2.5 V for different TCs under study, and the respective calculated τ_R values are presented in Figure 26. Generally, τ_R value increases at higher applied ΔE for ideally capacitive systems, i.e. without some additional fast faradaic reactions, which is valid also for the SCs under study (Figure 27). Data in Figures 26 and 27 show that the shortest τ_R were established for $NaPF_6$-2TC and $LiPF_6$-2TC, i.e. in case of Na- and Li-salts based on the symmetric PF_6^- anion of smallest effective size (including solvation shell). The somewhat longer τ_R values for $LiPF_6$-2TC compared to $NaPF_6$-2TC at different applied ΔE indicate that the diffusion of Na^+ ions should be faster in the micro-meso-porous carbon electrode structure. This effect can be explained by the lower solvation energy for Na^+ ions than that for Li^+ ions, and therefore by the smaller diameter of solvated (or partially solvated) Na^+ ions.

The low-frequency $|Q|/|S|$ value much lower than 100% confirms the beginning $LiClO_4$ electrolyte decomposition already at ΔE = 2.5 V, and thus having a τ_R more than two times longer than for the corresponding Na-salt based TC (Figure 26). $NaClO_4$-2TC has longer time constants at ΔE > 0.0 V compared to $NaPF_6$-2TC that could be explained by the PF_6^- weaker

coordinating ability, discussed earlier, and therefore higher mobility in the porous electrode matrix compared to ClO_4^- (Figures 26 and 27). The τ_R value calculated for the TC with Li-salt of asymmetric $B(C_2O_4)_2^-$ anion is equal to that of the $NaClO_4$-2TC at ΔE = 2.5 V. Even longer τ_R was obtained for the $CsCB_{11}H_{12}$-2TC probably due to the bulky $CB_{11}H_{12}^-$ anion. The effect of Cs^+ mobility could be better described if additional electrochemical measurements were made with, for example, $CsPF_6$ and $CsClO_4$ electrolytes. Two rather short τ_R values obtained for the $LiCF_3SO_3$-2TC indicate a complex two-step salt decomposition reaction.

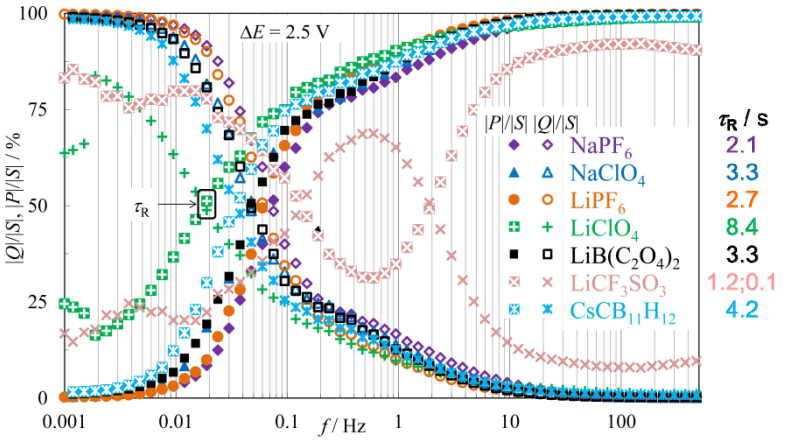

Figure 26. Dependence of normalized reactive power $|Q|/|S|$ and active power $|P|/|S|$ on ac frequency for different alkali salt based TCs at ΔE = 2.5 V.

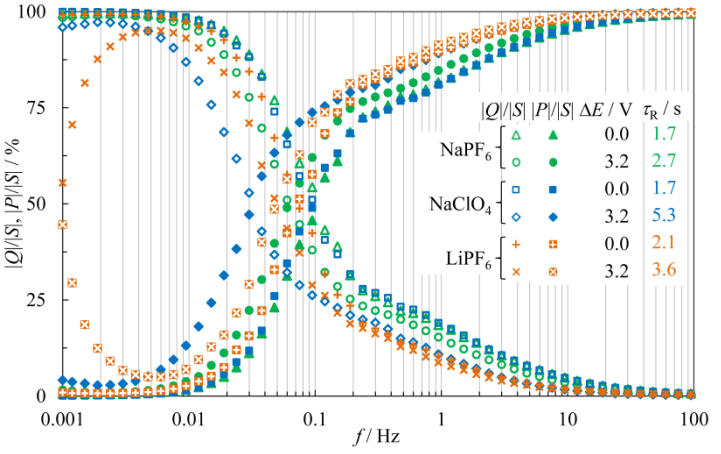

Figure 27. Dependence of normalized reactive power $|Q|/|S|$ and active power $|P|/|S|$ on ac frequency for $NaPF_6$-2TC, $NaClO_4$-2TC and $LiPF_6$-2TC at ΔE = 0.0 V and 3.2 V.

Calculated E_{max} and P_{max} for the TCs under study are presented in Figure 28. The highest E_{max} values of ~42 Wh kg^{-1} were obtained for $NaClO_4$-2TC, $LiB(C_2O_4)_2$-2TC and $CsCB_{11}H_{12}$-2TC, from which the latter two might be slightly overestimated due to the marked increase in C_s at ΔE > 2.5 V (Figure 19). The highest P_{max} values of ~95 and ~85 kW kg^{-1} were found for $NaPF_6$-2TC and $LiPF_6$-2TC, respectively. Due to faradaic decomposition, the calculations for $LiClO_4$-2TC and $LiCF_3SO_3$-2TC were made using EIS data at ΔE = 2.5 V instead of ΔE = 3.0 V. Taking also into account higher R_s (Figure 17b) and smaller C_s (Figure 19) values caused by surface blocking effect for these TCs, much smaller E_{max} and P_{max} were obtained. As the C_s variation at ΔE = 3.0 V is not very large between the TCs containing electrochemically stable electrolytes (Figure 19), the E_{max} has 20% difference from 35 to 42 Wh kg^{-1}, being more determined by the electrode materials used. However, the P_{max} values obtained differ up to 50%, ranging from 45 to 95 kW kg^{-1}, because R_s depend more strongly on the electrolyte used (Figure 17b).

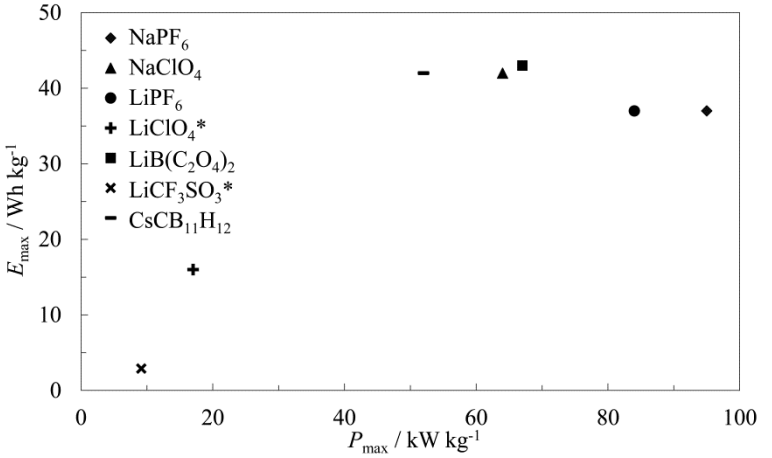

Figure 28. Calculated maximum energy and power density values for the studied TCs at ΔE = 3.0 V. * – ΔE = 2.5 V.

6.3. Life time tests of studied SCs

Life time tests were done for $NaClO_4$-2TC, $NaPF_6$-2TC and $LiB(C_2O_4)_2$-2TC by CCCD test between ΔE = 1.5…3.0 V at a constant current density of 4 mA cm^{-2} [98, 105]. In case of Na-salts based TCs the charge/discharge curves remained practically linear even after 5000 galvanic cycles (Figure 29, inset) and the *IR*-drop was practically constant from 2nd to 5000th cycle (~0.06 V). The difference between discharge C_{CCCD} values of 1st cycle and 5000th was 15% and 22% for $NaClO_4$-2TC and $NaPF_6$-2TC, respectively (Figure 29). For $LiB(C_2O_4)_2$-2TC, the CCCD curves are also almost linear after 5000 cycles, but the *IR*-drop is

higher and increases from ~0.1 to ~0.18 V during cell potential cycling [98]. The discharge capacitance loss was 33% during the time stability test, mainly caused by the faradaic processes starting to occur at $\Delta E \geq 2.5$ V. Good coulombic efficiency was established for the analyzed TCs as the values of charge/discharge C_{CCCD} ratio remained > 0.99 even after 5000 charge/discharge cycles.

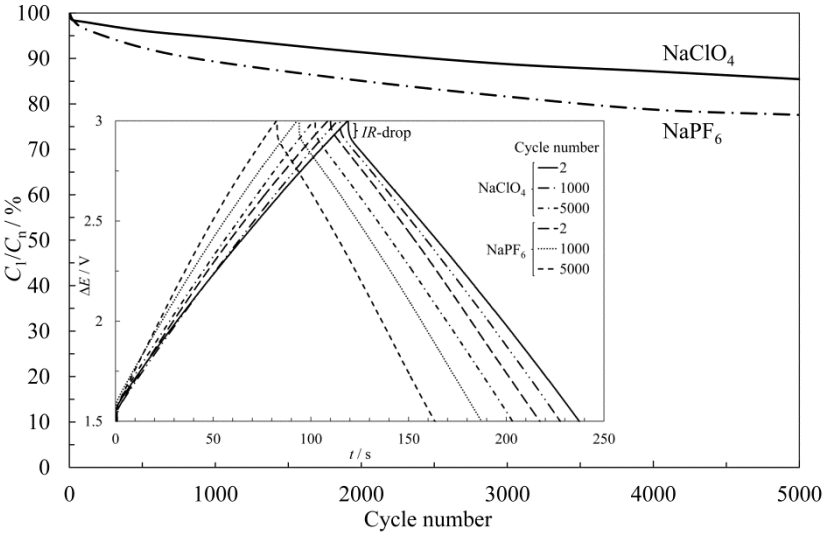

Figure 29. Ratio of discharge capacitances of 1st and nth cycle C_1/C_n vs. Cycle number and galvanic cycles (figure inset) for $NaClO_4$-2TC and $NaPF_6$-2TC at charge/discharge current density of 4 ma cm^{-2}.

$LiClO_4$-2TC life time was tested between ΔE = 0.0…2.7 V at 1 mA cm^{-2} [97]. The charging/discharging curves were asymmetrical and the capacitance (charge density) of the TC decreased by as much as ~70%, mainly caused by the continuous surface blocking due to faradaic decomposition reaction products at $\Delta E \geq 2.5$ V. Also the coulombic efficiency of the TC at the CCCD conditions was < 0.85, indicating that this electrolyte is not a good candidate for SC application.

7. SUMMARY

Several supercapacitor (SC) test cells were assembled and characterized by electrochemical methods like cyclic voltammetry (CV), electrochemical impedance spectroscopy (EIS) and constant current charge/discharge. High surface area ($S_{BET} \approx 1690$ m^2 g^{-1}) micro-meso-porous carbide-derived carbon powders, synthesized from TiC and Mo_2C, were applied as electrode materials, which have been proven to have high capacitance and long cycle life in commercially applied quaternary alkyl ammonium salts based non-aqueous electrolytes. Electrolytes consisting of alkali metal cation and different anion based salts – namely, lithium hexafluorophosphate ($LiPF_6$), lithium perchlorate ($LiClO_4$), lithium trifluoromethanesulfonate ($LiCF_3SO_3$), lithium bis(oxalato)borate ($LiB(C_2O_4)_2$), sodium hexafluorophosphate ($NaPF_6$), sodium perchlorate ($NaClO_4$), and cesium carborane ($CsCB_{11}H_{12}$) – in an environmentally friendly mixed carbonate solvent system of ethylene carbonate and dimethyl carbonate were tested as candidates for high performance SCs.

The widest region of ideal polarizability, i.e. the highest SC cell potential, was established in case of $NaPF_6$, being 3.4 V. Also $LiPF_6$ and $NaClO_4$ enable applying rather high cell potential of 3.2 V. The calculated limiting gravimetric capacitance of the SCs under study was up to ~130 F g^{-1}, correlating well between data from CV and EIS measurements. However, much smaller capacitance was obtained for $LiClO_4$ and $LiCF_3SO_3$ based SCs due to remarkable surface blocking effect by electrolyte decomposition products. Calculated maximum energy density values at 3.0 V cell potential varied only by 20% between the test systems (35–42 Wh kg^{-1}), thus being only slightly influenced by the electrolyte properties.

The dependence of high-frequency series resistance and mass transfer processes on the electrolyte salt composition was established by impedance spectroscopy measurements. The smallest high-frequency series resistance (~2 Ω cm^2), highest ac frequency of reaching nearly ideal capacitive behavior (~0.15 Hz) and lowest characteristic time constant (~2.1 s at 2.5 V) were found for $NaPF_6$ electrolyte based SC. For the electrolytes stable above 2.7 V, the sequence of increase in time constants was: $NaPF_6 < LiPF_6 < NaClO_4 \leq LiB(C_2O_4)_2 < CsCB_{11}H_{12}$, and the calculated power density values decreased in the same electrolyte order from 95 to 45 kW kg^{-1}, thus changing by ~50%.

Mathematical fitting of impedance data showed that the process with the highest resistance is diffusion-like mass transfer of the electrolyte in the porous electrode structure. Also the external double layer capacitance is up to an order of magnitude higher compared to the electrode surface film capacitance.

The capacitance of $NaClO_4$ based system decreased by 15% during 5000 charge/discharge cycles, whereas in case of $NaPF_6$ and $LiB(C_2O_4)_2$, the decrease was 22% and 33%, respectively.

To conclude, alkali metal salt based non-aqueous electrolytes are an interesting option for SCs, however, improvements in time stability have to be achieved for long-lasting applications.

8. REFERENCES

[1] B.E. Conway, Electrochemical Supercapacitors: Scientific Fundamentals and Technological Applications, Kluwer Academic/Plenum Publishers, New York, 1999.

[2] F. Béguin, E. Frackowiak, M. Lu (Eds.), Supercapacitors. Materials, Systems, and Applications, Weinheim, 2013.

[3] A.G. Pandolfo, A.F. Hollenkamp, J. Power Sources 157 (2006) 11–27.

[4] R. Kötz, M. Carlen, Electrochim. Acta 45 (2000) 2483–2498.

[5] P. Simon, Y. Gogotsi, Nat. Mater. 7 (2008) 845–854.

[6] Yu.M. Volfkovich, T.M. Serdyuk, Russ. J. Electrochem. 38 (2002) 935–958.

[7] P.L. Taberna, P. Simon, J.F. Fauvarque, J. Electrochem. Soc. 150 (2003) A292–A300.

[8] A. Burke, J. Power Sources 91 (2000) 37–50.

[9] J.R. Miller, P. Simon, Science 321 (2008) 651–652.

[10] J.R. Miller, A.F. Burke, Electrochem. Soc. Interface 17 (1) (2008) 53–57.

[11] P. Simon, A. Burke, Electrochem. Soc. Interface 17 (1) (2008) 38–43.

[12] M. Arulepp, L. Permann, J. Leis, A. Perkson, K. Rumma, A. Jänes, E. Lust, J. Power Sources 133 (2004) 320–328.

[13] A. Jänes, L. Permann, M. Arulepp, E. Lust, J. Electroanal. Chem. 569 (2004) 257–269.

[14] E. Lust, G. Nurk, A. Jänes, M. Arulepp, P. Nigu, P. Möller, S. Kallip, V. Sammelselg, J. Solid State Electrochem. 7 (2003) 91–105.

[15] D. Aurbach, in: Nonaqueous Electrochemistry, D. Aurbach, D. Orbakh (Eds.), Marcel Dekker, New York, 1999.

[16] G.-A. Nazri, G. Pistoia (Eds.), Lithium Batteries: Science and Technology, Kluwer Academic Publishers, New York, 2004.

[17] D. Aurbach, Y. Talyosef, B. Markovsky, E. Markevich, E. Zinigrad, L. Asraf, J.S. Gnanaraj, H.-J. Kim, Electrochim. Acta 50 (2004) 247–254.

[18] R. Marom, O. Haik, D. Aurbach, I.C. Halalay, J. Electrochem. Soc. 157 (2010) A972–A983.

[19] K. Xu, S.S. Zhang, U. Lee, J.L. Allen, T.R. Jow, J. Power Sources 146 (2005) 79–85.

[20] L. Yang, M.M. Furczon, A. Xiao, B.L. Lucht, Z. Zhang, D.P. Abraham, J. Power Sources 195 (2010) 1698–1705.

[21] L. Larush-Asraf, M. Biton, H. Teller, E. Zinigrad, D. Aurbach, J. Power Sources 174 (2007) 400–407.

[22] H.E. Becker, U.S. Patent 2 800 616 (to General Electric), 1957.

[23] Y. Gogotsi (Ed.), Nanomaterials Handbook, CRC Press Taylor & Francis Group, Florida, 2006.

[24] E. Eustache, R. Frappier, R.L. Porto, S. Bouhtiyya, J.-F. Pierson, T. Brousse, Electrochem. Commun. 28 (2013) 104–106.

[25] B.E. Conway, V. Birss, J. Wojtowicz, J. Power Sources 66 (1997) 1–14.

[26] M. Weissmann, O. Crosnier, T. Brousse, D. Bélanger, Electrochim. Acta 82 (2012) 250–256.

[27] E. Frackowiak, G. Lota, J. Machnikowski, C. Vix-Guterl, F. Béguin, Electrochim. Acta 51 (2006) 2209–2214.

[28] A. Rudge, J. Davey, I. Raistrick, S. Gottesfeld, J. Power Sources 47 (1994) 89–107.
[29] G. Lota, K. Fic, E. Frackowiak, Electrochem. Commun. 13 (2011) 38–41.
[30] K. Fic, E. Frackowiak, F. Béguin, J. Mater. Chem. 22 (2012) 24213–24223.
[31] B.E. Conway, J.O'M. Bockris, I.A. Ammar, Trans. Faraday Soc. 47 (1951) 756–766.
[32] H. Helmholtz, Ann. Phys. (Leipzig) 89 (1853) 211–233.
[33] A. Hamelin, T. Vitanov, E. Sevastyanov, A. Popov, J. Electroanal. Chem. 145 (1983) 225–264.
[34] B.B. Damaskin, O.A. Petrii, V.V. Batrakov, Adsorption of Organic Compounds on Electrodes, Plenum Press, New York, 1971.
[35] L.G. Gouy, J. de Phys. 9 (1910) 457–468.
[36] D.L. Chapman, Philos. Mag. 25 (1913) 475–481.
[37] O. Stern, Zeit. Elektrochem. 30 (1924) 508–511.
[38] D.C. Grahame, Chem. Rev. 41 (1947) 441–501.
[39] A. Hamelin, in: Modern Aspects of Electrochemistry, no. 16, B.E. Conway, R.E. White, J.O'M. Bockris (Eds.), Plenum Press, New York, 1985, pp. 1–102.
[40] O.K. Rice, Phys. Rev. 31 (1928) 1051–1059.
[41] L.H. Thomas, Proc. Cambridge Philos. Soc. 23 (1927) 542–548.
[42] E. Fermi, Atti. Accad. Naz. Lincei, Cl. Sci. Fis. Mat. Nat. Rend. 6 (1927) 602–607.
[43] S. Amokrane, J.P. Badiali, J. Electroanal. Chem. 266 (1989) 21–35.
[44] S. Amokrane, J.P. Badiali, in: Modern Aspects of Electrochemsitry, no. 22, J.O'M. Bockris, B.E. Conway, R.E. White (Eds.), Plenum Press, New York, 1992, pp. 1–95.
[45] H.D. Hurwitz, J. Electroanal. Chem. 10 (1965) 35–41.
[46] E. Dutkiewicz, R. Parsons J. Electroanal. Chem. 11 (1966) 100–110.
[47] M.V. Fedorov, A.A. Kornyshev, Electrochim. Acta 53 (2008) 6835–6840.
[48] K. Lust, M. Väärtnõu, E. Lust, J. Electroanal. Chem. 532 (2002) 303–318.
[49] L. Siinor, K. Lust, E. Lust, J. Electroanal. Chem. 601 (2007) 39–46.
[50] R. Jäger, E. Härk, P. Möller, J. Nerut, K. Lust, E. Lust, J. Electroanal. Chem. 566 (2004) 217–226.
[51] M.D. Levi, S. Sigalov, G. Salitra, D. Aurbach, J. Maier, Chem. Phys. Chem. 12 (2011) 854–862.
[52] F. Beck, H. Krohn, in: Proc. Electrochemical Society Symposium on The Electrochemistry of Carbon (1983), vol. 84–5, S. Sarangapani, J.R. Adridge, B. Schumm (Eds.), The Electrochemical Society, Pennington, Jew Jersey, 1984, p. 574.
[53] D. Aurbach, I. Weismann, A. Zaban, O. Chusid, Electrochim. Acta 39 (1994) 51–71.
[54] M. Winter, J.O. Besenhard, M.E. Spahr, P. Novak, Adv. Matter. 10 (1998) 725–763.
[55] A.M. Colclasure, K.A. Smith, R.J. Kee, Electrochim. Acta 58 (2011) 33–43.
[56] D. Aurbach, B. Markovsky, I. Weissman, E. Levi, Y. Ein-Eli, Electrochim. Acta 45 (1999) 67–86.
[57] E. Frackowiak, F. Béguin, Carbon 39 (2001) 937–950.
[58] G. Salitra, A. Soffer, L. Eliad, Y. Cohen, D. Aurbach, J. Electrochem. Soc. 147 (2000) 2486–2493.

[59] M. Eikerling, A. A. Kornyshev, E. Lust, J. Electrochem. Soc. 152 (2005) E24–E33.
[60] O. Barbieri, M. Hahn, A. Herzog, R. Kötz, Carbon 43 (2005) 1303–1310.
[61] F. Béguin, E. Frackowiak, Carbons for Electrochemical Energy Storage and Conversion Systems, CRC Press, New York, 2010.
[62] S. Biniak, A. Swiatkowski, M. Pakula, L.R. Radovic (Eds.), Chemistry and Physics of Carbon, Vol. 27, Marcel Dekker, New York, 2001.
[63] J. Chmiola, G. Yushin, Y. Gogotsi, C. Portet, P. Simon, P. L. Taberna, Science 313 (2006) 1760–1763.
[64] J. Leis, M. Arulepp, A. Kuura, M. Lätt, E. Lust, Carbon 44 (2006) 2122–2129.
[65] T. Thomberg, A. Jänes, E. Lust, J. Electroanal. Chem. 630 (2009) 55–62.
[66] T. Thomberg, H. Kurig, A. Jänes, E. Lust, Micropor. Mesopor. Mater. 141 (2011) 88–93.
[67] A. Jänes, T. Thomberg, H. Kurig, E. Lust, Carbon 47 (2009) 23–29.
[68] A. Jänes, L. Permann, M. Arulepp, E. Lust, Electrochem. Commun. 6 (2004) 313–318.
[69] Y. Gogotsi, A. Nikitin, H. Ye, W. Zhou, J.E. Fischer, B. Yi, H.C. Foley, M.W. Barsoum, Nat. Mater. 2 (2003) 591–594.
[70] S. Urbonaite, S. Wachtmeister, C. Mirguet, E. Coronel, W.Y. Zou, S. Csillag, G. Svensson, Carbon 45 (2007) 2047–2053.
[71] I. Tallo, T. Thomberg, K. Kontturi, A. Jänes, E. Lust, Carbon 49 (2011) 4427–4433.
[72] E.N. Hoffman, G. Yushin, T. El-Raghy, Y. Gogotsi, M.W. Barsoum, Micropor. Mesopor. Mater. 112 (2008) 526–532.
[73] S. Brunauer, P.H. Emmett, E.Teller, J. Am. Chem. Soc. 60 (1983) 309–319.
[74] S. Lowell, J.E. Shields, M.A. Thomas, M. Thommes, Characterization of Porous Solids and Powders: Surface Area, Pore Size and Density, Springer, The Netherlands, 2006.
[75] S. Lowell, J. Shields, G. Charalambous, J. Manzione, J. Colloid Interf. Sci. 86 (1982) 191–195.
[76] S.J. Gregg, K.S.W. Sing, Adsorption, Surface Area, and Porosity. Academic Press, London, 1982.
[77] J.H. de Boer, B.C. Lippens, B.G. Linsen, J.C.P. Broekhoff, A. van den Heuvel, Th.J. Osinga, J. Colloid Interf. Sci. 21 (1966) 405–414.
[78] R.W. Magee, Rubber Chemistry and Technology, vol. 68. no. 4, 1995, pp. 590–600.
[79] G. Halsey, J. Chem. Phys. 16 (1948) 931–937.
[80] W.D. Harkins, G. Jura, J. Am. Chem. Soc. 66 (1944) 1362–1366.
[81] R. Evans, U.M.B. Marconi, P. Tarzona, J. Chem. Phys. 84 (1986) 2376–2400.
[82] P.I. Ravikovitch, G.L. Haller, A.V. Neimark, Adv. Colloid Interf. Sci. 76–77 (1998) 203–226.
[83] M.M. Dubinin, L.V. Radushkevich, Dokl. Akad. Nauk. SSSR 55 (1947) 327–329.
[84] E.P. Barrett, L.G. Joyner, P.P. Halenda, J. Am. Chem. Soc. 73 (1951) 373–380.
[85] G. Horvath, K. Kawazoe, J. Chem. Eng. Jpn. 16 (1983) 470–475.
[86] A.V. Neimark, Y. Lin, P.I. Ravikovitch, M. Thommes, Carbon 47 (2009) 1617–1628.
[87] G.Y. Gor, M. Thommes, K.A. Cychosz, A.V. Neimark, Carbon 50 (2012) 1583–1590.

[88] M. Galiński, A. Lewandowski, I. Stepniak, Electrochim. Acta 51 (2006) 5567–5580.
[89] T. Tsuda, C. L. Hussey, Electrochem. Soc. Interface 1 (2007) 42–49.
[90] S. Zhang, N. Sun, X. He, X. Lu, X. Zhang, J. Phys. Chem. Ref. Data 35 (2006) 1475–1517.
[91] H. Kurig, M. Vestli, K. Tõnurist, A. Jänes, E. Lust, J. Electrochem. Soc. 159(7) (2012) A944–A951.
[92] H. Kurig, A. Jänes, E. Lust, J. Electrochem. Soc. 157 (2010) A272–A279.
[93] A. Jänes, E. Lust, Electrochem. Commun. 7 (2005) 510–514.
[94] A. Jänes, E. Lust, J. Electroanal. Chem. 588 (2006) 285–295.
[95] A. Laheäär, H. Kurig, A. Jänes, E. Lust, Electrochim. Acta 54 (2009) 4587–4594.
[96] A. Laheäär, A. Jänes, E. Lust, ECS Trans. 28(8) (2010) 65–75.
[97] A. Laheäär, A. Jänes, E. Lust, Electrochim. Acta 56 (2011) 9048–9055.
[98] A. Laheäär, A. Jänes, E. Lust, J. Electroanal. Chem. 669 (2012) 67–72.
[99] K. Xu, S. Zhang, B.A. Poese, T.R. Jow, Electrochem. Solid State Lett. 5(11) (2002) A259–A262.
[100] K. Xu, S. Zhang, T.R. Jow, W. Xu, C.A. Angell, Electrochem. Solid State Lett. 5(1) (2002) A26–A29.
[101] V. Khomenko, E. Raymundo-Piñero, F. Béguin, J. Power Sources 177 (2008) 643–651.
[102] S.R. Sivakkumar, J.Y. Nerkar, A.G. Pandolfo, Electrochim. Acta 55 (2010) 3330–3335.
[103] A.D. Pasquier, I. Plitz, S. Menocal, G. Amatucci, J. Power Sources 115 (2003) 171–178.
[104] S.R. Sivakkumar, A.G. Pandolfo, Electrochim. Acta 65 (2012) 280–287.
[105] A. Laheäär, A. Jänes, E. Lust, Electrochim. Acta 82 (2012) 309–313.
[106] A. Laheäär, A. Jänes, E. Lust, ECS Trans. 50(43) (2013) 153–161.
[107] D.A. Stevens, J.R. Dahn, J. Electrochem. Soc. 147 (2000) 1271–1273.
[108] K. Gotoh, T. Ishikawa, S. Shimadzu, N. Yabuuchi, S. Komaba, K. Takeda, A. Goto, K. Deguchi, S. Ohki, K. Hashi, T. Shimizu, H. Ishida, J. Power Sources 225 (2013) 137–140.
[109] K. Kuratani, M. Yao, H. Senoh, N. Takeichi, T. Sakai, T. Kiyobayashi, Electrochim. Acta 76 (2012) 320–325.
[110] S. Komaba, W. Murata, T. Ishikawa, N. Yabuuchi, T. Ozeki, T. Nakayama, A. Ogata, K. Gotoh, K. Fujiwara, Adv. Funct. Mater. 21 (2011) 3859–3867.
[111] M. Nishijima, I.D. Gocheva, S. Okada, T. Doi, J. Yamaki, T. Nishida, J. Power Sources 190 (2009) 558–562.
[112] S.S. Zhang, J. Power Sources 164 (2007) 351–364.
[113] K. Tõnurist, T. Thomberg, A. Jänes, I. Kink, E. Lust, Electrochem. Commun. 22 (2012) 77–80.
[114] K. Tõnurist, T. Thomberg, A. Jänes, E. Lust, J. Electrochem. Soc.160 (2013) A1–A9.
[115] A. Bard, L.R. Faulkner, Electrochemical methods. Fundamentals and Applications, John Wiley & Sons, New York, 1980.
[116] E. Barsoukov, J.R. Macdonald (Eds.), Impedance spectroscopy. Theory, Experiment, and Applications, 2nd ed., Wiley-Interscience, Hoboken, 2005.
[117] E. Lust, A. Jänes, T. Pärn, P. Nigu, J. Solid State Electrochem. 8 (2004) 224–237.

[118] M.E. Orazem, N. Pébère, B. Tribollet, J. Electrochem. Soc. 153 (2006) B129–B136.
[119] B. Hirschorn, M.E. Orazem, B. Tribollet, V. Vivier, I. Frateur, M. Musiani, J. Electrochem. Soc. 157 (2010) C452–C457.
[120] J.-P. Randin, E.B. Yeager, J. Electrochem. Soc. 118 (1971) 711–714.
[121] M.D. Levi, D. Aurbach, J. Phys. Chem. B 108 (2004) 11693–11703.
[122] M. Itagaki, S. Suzuki, I. Shitanda, K. Watanabe, H. Nakazawa, J. Power Sources 164 (2007) 415–424.
[123] J.P. Meyers, M. Doyle, R.M. Darling, J. Newman, J. Electrochem. Soc. 147 (8) (2000) 2930–2940.
[124] J.-P. Randin, E.B. Yeager, J. Electroanal. Chem. 38 (1972) 257–276.
[125] S. Trasatti, E. Lust, in: Modern Aspects of Electrochemistry, no. 33, R.E. White, J.O'M. Bockris, B.E. Conway (Eds.), Kluwer/Plenum, New York, 1999, pp. 1–216.
[126] H. Gerischer, R. McIntyre, D. Scherson, W. Storck, J. Phys. Chem. 91 (1987) 1930–1935.
[127] ZView for Windows (versions 2.8d and 3.2c), Scribner Associates, Inc., Southern Pines, NC.
[128] T. Jacobsen, K. West, Electrochim. Acta 40 (1995) 255–262.
[129] A. Compte, Phys. Rev. E 53 (1996) 4191–4193.
[130] J. Bisquert, G. Garcia-Belmonte, P. Bueno, E. Longo, L.O.S. Bulhões, J. Electroanal. Chem. 452 (1998) 229–234.
[131] J. Jamnik, J. Maier, Phys. Chem. Chem. Phys. 3 (2001) 1668–1678.
[132] A.N. Frumkin, V.I. Melik-Gaykazyan, Dokl. Akad. Nauk. 77 (1951) 855–858.
[133] A.N. Frumkin, B.B. Damaskin, in: Modern Aspects of Electrochemistry, no. 3, J.O'M. Bockris, B.E. Conway (Eds.), Butterworth, London, 1964, p. 149.
[134] Y.A. Maletin, N.G. Strizhakova, V.Y. Izotov, A.A. Mironova, S.G. Kozachkov, V.V. Danilin, S.N. Podmogilny, M. Arulepp, J.A. Kukushkina, A.J. Kravchik, V.V. Sokolov, A. Perkson, J. Leis, J. Zheng, S.K. Gordeev, J.Y. Kolotilova, J. Cederström, C.L. Wallace, US Patent No: 6,602,742.
[135] R.J. Nemanich, S.A. Solin, Phys. Rev. B 20 (1979) 392–401.
[136] A.C. Ferrari, J. Robertson, Phys. Rev. B 61 (2000) 14095–14107.
[137] S. Urbonaite, L. Hälldahl, G. Svensson, Carbon 46 (2008) 1942–1947.
[138] M.S. Dresselhaus, G. Dresselhaus, M. Hofman, Vib. Spectrosc. 45 (2007) 71–81.
[139] J.F. Hinton, E.S. Amis, Chem. Rev. 71 (1971) 627–674.
[140] D. Michael, P. Mingos, A.L. Rohl, Inorg. Chem. 30 (1991) 3769–3771.
[141] H.G. Mayfield, W.E. Bull, J. Chem. Soc. A (1971) 2279–2281.
[142] M. Ue, J. Electrochem. Soc. 141 (1994) 3336–3342.
[143] D.M. Seo, O. Borodin, D. Balogh, M. O'Connell, Q. Ly, S.-D. Han, S. Passerini, W.A. Henderson, J. Electrochem. Soc. 160 (8) (2013) A1061–A1070.
[144] J.-C. Panitz, U. Wietelmann, M. Wachtler, S. Ströbele, M. Wohlfahrt-Mehrens, J. Power Sources 153 (2006) 396–401.
[145] D. Aurbach, M.D. Levi, G. Salitra, N. Levy, E. Pollak, J. Muthu, J. Electrochem. Soc. 155 (2008) A745–A753.

9. SUMMARY IN ESTONIAN

Leelismetallide sooladel põhinevate superkondensaatori mittevesilahuse elektrolüütide elektrokeemiline karakteriseerimine

Käesolevas doktoritöös komplekteeriti mitmed erinevad superkondensaatori (SK) testsüsteemid, mille elektrokeemilisi omadusi uuriti tsüklilise voltammeetria (CV), elektrokeemilise impedants-spektroskoopia (EIS) ja konstantsel voolul laadimise/tühjenemise meetoditega. Elektroodimaterjalidena kasutati TiC ja Mo_2C karbiididest sünteesitud suure eripinnaga mikro-meso-poorseid süsinikpulbreid ($S_{BET} \approx 1690\ m^2\ g^{-1}$), millel on kommertsiaalselt rakendatavates kvaternaarsetel alküülammoonium-sooladel põhinevates elektrolüütides suur mahtuvus ning pikk eluiga. Uuriti uudsete elektrolüütide rakendatavust SK-des, mis koosnevad leelismetallide katioonidel ning erinevatel anioonidel põhinevate soolade – liitium-heksafluorofosfaat ($LiPF_6$), liitiumperkloraat ($LiClO_4$), liitiumtrifluorometaansulfonaat ($LiCF_3SO_3$), liitium-bis(oksalaato)boraat ($LiB(C_2O_4)_2$), naatrium-heksafluorofosfaat ($NaPF_6$), naatriumperkloraat ($NaClO_4$) ja tseesiumkarboraan ($CsCB_{11}H_{12}$) – lahustest keskkonnasõbralikumas etüleenkarbonaadi ja dimetüülkarbonaadi solventsegus.

Väga lai ideaalse polariseeritavuse ala ehk kõrgeim rakupotentsiaal 3,4 V saavutati $NaPF_6$ korral. Ka $LiPF_6$ ja $NaClO_4$ võimaldavad rakendada kõrget rakupotentsiaali kuni 3,2 V. SK süsteemide piiriliseks mahtuvuseks arvutati nii CV kui ka EIS andmetest kuni ~130 F g^{-1}. Samas $LiClO_4$ ja $LiCF_3SO_3$ sooladega SK-de mahtuvus saadi elektrolüüdi laguproduktide poolt pinna märgatava blokeerumise tõttu tunduvalt madalam. Arvutatud kõrged energiatiheduse väärtused olid ainult mõnevõrra mõjutatud kasutatavast elektrolüüdist ning varieerusid testsüsteemide ulatuses 20% (35–42 Wh kg^{-1}).

Kõrgsagedusliku järjestiktakistuse ning massiülekande takistuse sõltuvus elektrolüüdi soola keemilisest koostisest määrati EIS andmetest. Madalaim kõrgsageduslik järjestiktakistus (~2 Ω cm^2), kõrgeim ideaalsele mahtuvuslikule käitumisele jõudmise sagedus (~0,15 Hz) ning lühim karakteerne ajakonstant (2,5 V juures ~2,1 s) määrati $NaPF_6$ elektrolüüdiga SK korral. Ajakonstandid pikenesid elektrokeemiliselt stabiilsete elektrolüütide reas $NaPF_6 < LiPF_6 < NaClO_4 \leq LiB(C_2O_4)_2 < CsCB_{11}H_{12}$ ning võimsustihedused kahanesid samas järjestuses väärtuselt 95 kuni 45 kW kg^{-1}, muutudes seega ~50% ulatuses.

EIS andmete modelleerimise põhjal oli kõige suurema takistusega protsess uuritud süsteemides elektrolüüdi difusiooniline massiülekanne elektroodi poorses struktuuris. Elektroodide makropoorsetel pindadel moodustunud kaksikkihi mahtuvus oli kuni suurusjärk suurem, võrreldes elektroodi pinnale moodustunud pindkihi kõrgsagedusliku mahtuvusega.

$NaClO_4$ soolal põhineva SK mahtuvus vähenes 5000 laadimise/tühjenemise tsükli käigus 15% ning $NaClO_4$ ja $LiB(C_2O_4)_2$ korral vastavalt 22% ja 33%.

Kokkuvõttes on leelismetallide sooladel põhinevad mittevesilahuse elektrolüüdid huvitav valik SK-des rakendamiseks, kuigi nende ajaline stabiilsus vajab kauakestvateks rakendusteks edasist optimeerimist.

10. ACKNOWLEDGEMENTS

First and foremost, I would like to express my greatest gratitude to my supervisors Professor Enn Lust and Ph.D. Alar Jänes for their continuous encouragement, for all the interesting discussions throughout the years and for setting an example as outstanding scientists.

Several coworkers have played an important role in my experimental work. Thanks to Rait Kanarbik for SEM images and for being my 'emergency person' for countless times, Tavo Romann for depositing aluminium current collectors by magnetron sputtering, Heisi Kurig for gas sorption measurements, Indrek Tallo and Thomas Thomberg for synthesizing CDC powders. Thanks to all my colleagues for their support, good advice and absolutely enjoyable company.

I am indescribably grateful to my family for always believing in me, being proud of my achievements and for their unconditional love. And last but not least, my warmest thanks go to my close friends who have been there for me through both cheerful and complicated times, have appreciated me as I am and have given me lots of precious memories. You are my greatest treasure.

This work has been supported by Estonian Science Foundation (grants no. 6696, 7606 and 8172), Estonian Ministry of Education and Research (project SF0180002s08), graduate school 'Functional materials and processes' (European Social Fund project 1.2.0401.09-0079), European Regional Development Fund: Estonian Materials Technology project (3.2.1101.12-0019), Estonian Centres of Excellence in Research project (3.2.0101-0030), and Estonian Energy Technology project (3.2.0501.10-0015).

11. PUBLICATIONS

CURRICULUM VITAE

Name: Ann Laheäär
Date of birth: October 8,1985
Citizenship: Estonian
Contact: Institute of Chemistry, Faculty of Science and Technology, University of Tartu
14a Ravila Street, 50411 Tartu, Estonia
E-mail: laheann@gmail.com

Education and professional employment:

2002–2005	Tallinn Secondary Science School (*cum laude*)
2005–2008	University of Tartu – Bachelor's degree in chemistry
2008–2009	University of Tartu – Master's degree in chemistry (*cum laude*)
2009–	University of Tartu, Institute of Chemistry, PhD student
2012	University of Orléans (France), CNRS, visiting PhD student
2008–2010	University of Tartu, Institute of Chemistry, laboratorian
2010–	University of Tartu, Institute of Chemistry, chemist

Awards:

2009	Foundation Archimedes, National contest of students researches, I prize in the field of natural science and technics in Master's study level

List of Publications

1. A. Laheäär, A. Jänes, E. Lust, Novel $NaClO_4$ and $NaPF_6$ Based Non-Aqueous Electrolytes for Electrical Double Layer Capacitor Application. ECS Transactions 50(43) (2013) 153–161.
2. A. Laheäär, A.-L. Peikolainen, M. Koel, A. Jänes, E. Lust, Comparison of carbon aerogel and carbide-derived carbon as electrode materials for non-aqueous supercapacitors with high performance. Journal of Solid State Electrochemistry 16(8) (2012) 2717–2722.
3. A. Laheäär, A. Jänes, E. Lust, Lithium bis(oxalato) borate as an electrolyte for micromesoporous carbide-derived carbon based supercapacitors. Journal of Electroanalytical Chemistry 669 (2012) 67–72.
4. A. Laheäär, A. Jänes, E. Lust, $NaClO_4$ and $NaPF_6$ as potential non-aqueous electrolyte salts for electrical double layer capacitor application. Electrochimica Acta 82 (2012) 309–313.
5. A. Laheäär, A. Jänes, E. Lust, Electrochemical properties of carbide-derived carbon electrodes in non-aqueous electrolytes based on different Li-salts. Electrochimica Acta 56 (2011) 9048–9055.
6. A. Laheäär, A. Jänes, E. Lust, Electrochemical Behavior of Carbide Derived Carbons in $LiPF_6$ and $LiCF_3SO_3$ Nonaqueous Electrolytes. ECS Transactions 28(8) (2010) 65–75.

7. A. Laheäär, H. Kurig, A. Jänes, E. Lust, $LiPF_6$ based ethylene carbonate – dimethyl carbonate electrolyte for high power density electrical double layer capacitor. Electrochimica Acta 54 (2009) 4587–4594.
8. A. Jänes, T. Thomberg, K. Tõnurist, H. Kurig, A. Laheäär, E. Lust, Micro- and Mesoporous Carbide-Derived Carbon Materials and Polymer Membranes for Supercapacitors. ECS Transactions 16(1) (2008) 57–67.

ELULOOKIRJELDUS

Nimi: Ann Laheäär
Sünniaeg: 8. oktoober 1985
Kodakondsus: Eesti
Kontakt: Keemia instituut, loodus-ja tehnoloogiateaduskond,
Tartu Ülikool
Ravila 14a, 50411 Tartu, Eesti
E-post: laheann@gmail.com

Haridus ning erialane teenistuskäik:

2002–2005	Tallinna Reaalkool (*cum laude*)
2005–2008	Tartu Ülikool – bakalaureusekraad keemias
2008–2009	Tartu Ülikool – magistrikraad keemias (*cum laude*)
2009–	Tartu Ülikooli keemia instituut, doktorant
2012	Orléans'i Ülikool (Prantsusmaa), CNRS, külalis-doktorant
2008–2010	Tartu Ülikooli keemia instituut, laborant
2010–	Tartu Ülikooli keemia instituut, keemik

Auhinnad:

2009	Sihtasutus Archimedes, Üliõpilaste teadustööde riiklikul konkurssil I koht loodus-teaduste ja tehnika valdkonnas magistriõppe tasemel

Teaduspublikatsioonid:

1. A. Laheäär, A. Jänes, E. Lust, Novel $NaClO_4$ and $NaPF_6$ Based Non-Aqueous Electrolytes for Electrical Double Layer Capacitor Application. ECS Transactions 50(43) (2013) 153–161.
2. A. Laheäär, A.-L. Peikolainen, M. Koel, A. Jänes, E. Lust, Comparison of carbon aerogel and carbide-derived carbon as electrode materials for non-aqueous supercapacitors with high performance. Journal of Solid State Electrochemistry 16(8) (2012) 2717–2722.
3. A. Laheäär, A. Jänes, E. Lust, Lithium bis(oxalato) borate as an electrolyte for micromesoporous carbide-derived carbon based supercapacitors. Journal of Electroanalytical Chemistry 669 (2012) 67–72.
4. A. Laheäär, A. Jänes, E. Lust, $NaClO_4$ and $NaPF_6$ as potential non-aqueous electrolyte salts for electrical double layer capacitor application. Electrochimica Acta 82 (2012) 309–313.
5. A. Laheäär, A. Jänes, E. Lust, Electrochemical properties of carbide-derived carbon electrodes in non-aqueous electrolytes based on different Li-salts. Electrochimica Acta 56 (2011) 9048–9055.
6. A. Laheäär, A. Jänes, E. Lust, Electrochemical Behavior of Carbide Derived Carbons in $LiPF_6$ and $LiCF_3SO_3$ Nonaqueous Electrolytes. ECS Transactions 28(8) (2010) 65–75.

7. A. Laheäär, H. Kurig, A. Jänes, E. Lust, $LiPF_6$ based ethylene carbonate – dimethyl carbonate electrolyte for high power density electrical double layer capacitor. Electrochimica Acta 54 (2009) 4587–4594.
8. A. Jänes, T. Thomberg, K. Tõnurist, H. Kurig, A. Laheäär, E. Lust, Micro- and Mesoporous Carbide-Derived Carbon Materials and Polymer Membranes for Supercapacitors. ECS Transactions 16(1) (2008) 57–67.

DISSERTATIONES CHIMICAE UNIVERSITATIS TARTUENSIS

1. **Toomas Tamm.** Quantum-chemical simulation of solvent effects. Tartu, 1993, 110 p.
2. **Peeter Burk.** Theoretical study of gas-phase acid-base equilibria. Tartu, 1994, 96 p.
3. **Victor Lobanov.** Quantitative structure-property relationships in large descriptor spaces. Tartu, 1995, 135 p.
4. **Vahur Mäemets.** The ^{17}O and ^{1}H nuclear magnetic resonance study of H_2O in individual solvents and its charged clusters in aqueous solutions of electrolytes. Tartu, 1997, 140 p.
5. **Andrus Metsala.** Microcanonical rate constant in nonequilibrium distribution of vibrational energy and in restricted intramolecular vibrational energy redistribution on the basis of slater's theory of unimolecular reactions. Tartu, 1997, 150 p.
6. **Uko Maran.** Quantum-mechanical study of potential energy surfaces in different environments. Tartu, 1997, 137 p.
7. **Alar Jänes.** Adsorption of organic compounds on antimony, bismuth and cadmium electrodes. Tartu, 1998, 219 p.
8. **Kaido Tammeveski.** Oxygen electroreduction on thin platinum films and the electrochemical detection of superoxide anion. Tartu, 1998, 139 p.
9. **Ivo Leito.** Studies of Brønsted acid-base equilibria in water and non-aqueous media. Tartu, 1998, 101 p.
10. **Jaan Leis.** Conformational dynamics and equilibria in amides. Tartu, 1998, 131 p.
11. **Toonika Rinken.** The modelling of amperometric biosensors based on oxidoreductases. Tartu, 2000, 108 p.
12. **Dmitri Panov.** Partially solvated Grignard reagents. Tartu, 2000, 64 p.
13. **Kaja Orupõld.** Treatment and analysis of phenolic wastewater with microorganisms. Tartu, 2000, 123 p.
14. **Jüri Ivask.** Ion Chromatographic determination of major anions and cations in polar ice core. Tartu, 2000, 85 p.
15. **Lauri Vares.** Stereoselective Synthesis of Tetrahydrofuran and Tetrahydropyran Derivatives by Use of Asymmetric Horner-Wadsworth-Emmons and Ring Closure Reactions. Tartu, 2000, 184 p.
16. **Martin Lepiku.** Kinetic aspects of dopamine D_2 receptor interactions with specific ligands. Tartu, 2000, 81 p.
17. **Katrin Sak.** Some aspects of ligand specificity of P2Y receptors. Tartu, 2000, 106 p.
18. **Vello Pällin.** The role of solvation in the formation of iotsitch complexes. Tartu, 2001, 95 p.

19. **Katrin Kollist.** Interactions between polycyclic aromatic compounds and humic substances. Tartu, 2001, 93 p.
20. **Ivar Koppel.** Quantum chemical study of acidity of strong and superstrong Brønsted acids. Tartu, 2001, 104 p.
21. **Viljar Pihl.** The study of the substituent and solvent effects on the acidity of OH and CH acids. Tartu, 2001, 132 p.
22. **Natalia Palm.** Specification of the minimum, sufficient and significant set of descriptors for general description of solvent effects. Tartu, 2001, 134 p.
23. **Sulev Sild.** QSPR/QSAR approaches for complex molecular systems. Tartu, 2001, 134 p.
24. **Ruslan Petrukhin.** Industrial applications of the quantitative structure-property relationships. Tartu, 2001, 162 p.
25. **Boris V. Rogovoy.** Synthesis of (benzotriazolyl)carboximidamides and their application in relations with *N*- and *S*-nucleophyles. Tartu, 2002, 84 p.
26. **Koit Herodes.** Solvent effects on UV-vis absorption spectra of some solvatochromic substances in binary solvent mixtures: the preferential solvation model. Tartu, 2002, 102 p.
27. **Anti Perkson.** Synthesis and characterisation of nanostructured carbon. Tartu, 2002, 152 p.
28. **Ivari Kaljurand.** Self-consistent acidity scales of neutral and cationic Brønsted acids in acetonitrile and tetrahydrofuran. Tartu, 2003, 108 p.
29. **Karmen Lust.** Adsorption of anions on bismuth single crystal electrodes. Tartu, 2003, 128 p.
30. **Mare Piirsalu.** Substituent, temperature and solvent effects on the alkaline hydrolysis of substituted phenyl and alkyl esters of benzoic acid. Tartu, 2003, 156 p.
31. **Meeri Sassian.** Reactions of partially solvated Grignard reagents. Tartu, 2003, 78 p.
32. **Tarmo Tamm.** Quantum chemical modelling of polypyrrole. Tartu, 2003. 100 p.
33. **Erik Teinemaa.** The environmental fate of the particulate matter and organic pollutants from an oil shale power plant. Tartu, 2003. 102 p.
34. **Jaana Tammiku-Taul.** Quantum chemical study of the properties of Grignard reagents. Tartu, 2003. 120 p.
35. **Andre Lomaka.** Biomedical applications of predictive computational chemistry. Tartu, 2003. 132 p.
36. **Kostyantyn Kirichenko.** Benzotriazole – Mediated Carbon–Carbon Bond Formation. Tartu, 2003. 132 p.
37. **Gunnar Nurk.** Adsorption kinetics of some organic compounds on bismuth single crystal electrodes. Tartu, 2003, 170 p.
38. **Mati Arulepp.** Electrochemical characteristics of porous carbon materials and electrical double layer capacitors. Tartu, 2003, 196 p.

39. **Dan Cornel Fara.** QSPR modeling of complexation and distribution of organic compounds. Tartu, 2004, 126 p.
40. **Riina Mahlapuu.** Signalling of galanin and amyloid precursor protein through adenylate cyclase. Tartu, 2004, 124 p.
41. **Mihkel Kerikmäe.** Some luminescent materials for dosimetric applications and physical research. Tartu, 2004, 143 p.
42. **Jaanus Kruusma.** Determination of some important trace metal ions in human blood. Tartu, 2004, 115 p.
43. **Urmas Johanson.** Investigations of the electrochemical properties of polypyrrole modified electrodes. Tartu, 2004, 91 p.
44. **Kaido Sillar.** Computational study of the acid sites in zeolite ZSM-5. Tartu, 2004, 80 p.
45. **Aldo Oras.** Kinetic aspects of dATPαS interaction with $P2Y_1$ receptor. Tartu, 2004, 75 p.
46. **Erik Mölder.** Measurement of the oxygen mass transfer through the air-water interface. Tartu, 2005, 73 p.
47. **Thomas Thomberg.** The kinetics of electroreduction of peroxodisulfate anion on cadmium (0001) single crystal electrode. Tartu, 2005, 95 p.
48. **Olavi Loog.** Aspects of condensations of carbonyl compounds and their imine analogues. Tartu, 2005, 83 p.
49. **Siim Salmar.** Effect of ultrasound on ester hydrolysis in aqueous ethanol. Tartu, 2006, 73 p.
50. **Ain Uustare.** Modulation of signal transduction of heptahelical receptors by other receptors and G proteins. Tartu, 2006, 121 p.
51. **Sergei Yurchenko.** Determination of some carcinogenic contaminants in food. Tartu, 2006, 143 p.
52. **Kaido Tämm.** QSPR modeling of some properties of organic compounds. Tartu, 2006, 67 p.
53. **Olga Tšubrik.** New methods in the synthesis of multisubstituted hydrazines. Tartu. 2006, 183 p.
54. **Lilli Sooväli.** Spectrophotometric measurements and their uncertainty in chemical analysis and dissociation constant measurements. Tartu, 2006, 125 p.
55. **Eve Koort.** Uncertainty estimation of potentiometrically measured ph and pK_a values. Tartu, 2006, 139 p.
56. **Sergei Kopanchuk.** Regulation of ligand binding to melanocortin receptor subtypes. Tartu, 2006, 119 p.
57. **Silvar Kallip.** Surface structure of some bismuth and antimony single crystal electrodes. Tartu, 2006, 107 p.
58. **Kristjan Saal.** Surface silanization and its application in biomolecule coupling. Tartu, 2006, 77 p.
59. **Tanel Tätte.** High viscosity $Sn(OBu)_4$ oligomeric concentrates and their applications in technology. Tartu, 2006, 91 p.

60. **Dimitar Atanasov Dobchev**. Robust QSAR methods for the prediction of properties from molecular structure. Tartu, 2006, 118 p.
61. **Hannes Hagu**. Impact of ultrasound on hydrophobic interactions in solutions. Tartu, 2007, 81 p.
62. **Rutha Jäger.** Electroreduction of peroxodisulfate anion on bismuth electrodes. Tartu, 2007, 142 p.
63. **Kaido Viht.** Immobilizable bisubstrate-analogue inhibitors of basophilic protein kinases: development and application in biosensors. Tartu, 2007, 88 p.
64. **Eva-Ingrid Rõõm.** Acid-base equilibria in nonpolar media. Tartu, 2007, 156 p.
65. **Sven Tamp.** DFT study of the cesium cation containing complexes relevant to the cesium cation binding by the humic acids. Tartu, 2007, 102 p.
66. **Jaak Nerut.** Electroreduction of hexacyanoferrate(III) anion on Cadmium (0001) single crystal electrode. Tartu, 2007, 180 p.
67. **Lauri Jalukse.** Measurement uncertainty estimation in amperometric dissolved oxygen concentration measurement. Tartu, 2007, 112 p.
68. **Aime Lust.** Charge state of dopants and ordered clusters formation in CaF_2:Mn and CaF_2:Eu luminophors. Tartu, 2007, 100 p.
69. **Iiris Kahn**. Quantitative Structure-Activity Relationships of environmentally relevant properties. Tartu, 2007, 98 p.
70. **Mari Reinik.** Nitrates, nitrites, N-nitrosamines and polycyclic aromatic hydrocarbons in food: analytical methods, occurrence and dietary intake. Tartu, 2007, 172 p.
71. **Heili Kasuk.** Thermodynamic parameters and adsorption kinetics of organic compounds forming the compact adsorption layer at Bi single crystal electrodes. Tartu, 2007, 212 p.
72. **Erki Enkvist.** Synthesis of adenosine-peptide conjugates for biological applications. Tartu, 2007, 114 p.
73. **Svetoslav Hristov Slavov**. Biomedical applications of the QSAR approach. Tartu, 2007, 146 p.
74. **Eneli Härk.** Electroreduction of complex cations on electrochemically polished Bi(*hkl*) single crystal electrodes. Tartu, 2008, 158 p.
75. **Priit Möller.** Electrochemical characteristics of some cathodes for medium temperature solid oxide fuel cells, synthesized by solid state reaction technique. Tartu, 2008, 90 p.
76. **Signe Viggor.** Impact of biochemical parameters of genetically different pseudomonads at the degradation of phenolic compounds. Tartu, 2008, 122 p.
77. **Ave Sarapuu.** Electrochemical reduction of oxygen on quinone-modified carbon electrodes and on thin films of platinum and gold. Tartu, 2008, 134 p.
78. **Agnes Kütt.** Studies of acid-base equilibria in non-aqueous media. Tartu, 2008, 198 p.

79. **Rouvim Kadis.** Evaluation of measurement uncertainty in analytical chemistry: related concepts and some points of misinterpretation. Tartu, 2008, 118 p.
80. **Valter Reedo.** Elaboration of IVB group metal oxide structures and their possible applications. Tartu, 2008, 98 p.
81. **Aleksei Kuznetsov.** Allosteric effects in reactions catalyzed by the cAMP-dependent protein kinase catalytic subunit. Tartu, 2009, 133 p.
82. **Aleksei Bredihhin.** Use of mono- and polyanions in the synthesis of multisubstituted hydrazine derivatives. Tartu, 2009, 105 p.
83. **Anu Ploom.** Quantitative structure-reactivity analysis in organosilicon chemistry. Tartu, 2009, 99 p.
84. **Argo Vonk.** Determination of adenosine A_{2A}- and dopamine D_1 receptor-specific modulation of adenylate cyclase activity in rat striatum. Tartu, 2009, 129 p.
85. **Indrek Kivi.** Synthesis and electrochemical characterization of porous cathode materials for intermediate temperature solid oxide fuel cells. Tartu, 2009, 177 p.
86. **Jaanus Eskusson.** Synthesis and characterisation of diamond-like carbon thin films prepared by pulsed laser deposition method. Tartu, 2009, 117 p.
87. **Marko Lätt.** Carbide derived microporous carbon and electrical double layer capacitors. Tartu, 2009, 107 p.
88. **Vladimir Stepanov.** Slow conformational changes in dopamine transporter interaction with its ligands. Tartu, 2009, 103 p.
89. **Aleksander Trummal.** Computational Study of Structural and Solvent Effects on Acidities of Some Brønsted Acids. Tartu, 2009, 103 p.
90. **Eerold Vellemäe.** Applications of mischmetal in organic synthesis. Tartu, 2009, 93 p.
91. **Sven Parkel.** Ligand binding to 5-HT_{1A} receptors and its regulation by Mg^{2+} and Mn^{2+}. Tartu, 2010, 99 p.
92. **Signe Vahur.** Expanding the possibilities of ATR-FT-IR spectroscopy in determination of inorganic pigments. Tartu, 2010, 184 p.
93. **Tavo Romann**. Preparation and surface modification of bismuth thin film, porous, and microelectrodes. Tartu, 2010, 155 p.
94. **Nadežda Aleksejeva.** Electrocatalytic reduction of oxygen on carbon nanotube-based nanocomposite materials. Tartu, 2010, 147 p.
95. **Marko Kullapere.** Electrochemical properties of glassy carbon, nickel and gold electrodes modified with aryl groups. Tartu, 2010, 233 p.
96. **Liis Siinor.** Adsorption kinetics of ions at Bi single crystal planes from aqueous electrolyte solutions and room-temperature ionic liquids. Tartu, 2010, 101 p.
97. **Angela Vaasa.** Development of fluorescence-based kinetic and binding assays for characterization of protein kinases and their inhibitors. Tartu 2010, 101 p.

98. **Indrek Tulp.** Multivariate analysis of chemical and biological properties. Tartu 2010, 105 p.
99. **Aare Selberg.** Evaluation of environmental quality in Northern Estonia by the analysis of leachate. Tartu 2010, 117 p.
100. **Darja Lavõgina.** Development of protein kinase inhibitors based on adenosine analogue-oligoarginine conjugates. Tartu 2010, 248 p.
101. **Laura Herm.** Biochemistry of dopamine D_2 receptors and its association with motivated behaviour. Tartu 2010, 156 p.
102. **Terje Raudsepp.** Influence of dopant anions on the electrochemical properties of polypyrrole films. Tartu 2010, 112 p.
103. **Margus Marandi.** Electroformation of Polypyrrole Films: *In-situ* AFM and STM Study. Tartu 2011, 116 p.
104. **Kairi Kivirand.** Diamine oxidase-based biosensors: construction and working principles. Tartu, 2011, 140 p.
105. **Anneli Kruve.** Matrix effects in liquid-chromatography electrospray mass-spectrometry. Tartu, 2011, 156 p.
106. **Gary Urb.** Assessment of environmental impact of oil shale fly ash from PF and CFB combustion. Tartu, 2011, 108 p.
107. **Nikita Oskolkov.** A novel strategy for peptide-mediated cellular delivery and induction of endosomal escape. Tartu, 2011, 106 p.
108. **Dana Martin.** The QSPR/QSAR approach for the prediction of properties of fullerene derivatives. Tartu, 2011, 98 p.
109. **Säde Viirlaid.** Novel glutathione analogues and their antioxidant activity. Tartu, 2011, 106 p.
110. **Ülis Sõukand.** Simultaneous adsorption of Cd^{2+}, Ni^{2+}, and Pb^{2+} on peat. Tartu, 2011, 124 p.
111. **Lauri Lipping.** The acidity of strong and superstrong Brønsted acids, an outreach for the "limits of growth": a quantum chemical study. Tartu, 2011, 124 p.
112. **Heisi Kurig.** Electrical double-layer capacitors based on ionic liquids as electrolytes. Tartu, 2011, 146 p.
113. **Marje Kasari.** Bisubstrate luminescent probes, optical sensors and affinity adsorbents for measurement of active protein kinases in biological samples. Tartu, 2012, 126 p.
114. **Kalev Takkis.** Virtual screening of chemical databases for bioactive molecules. Tartu, 2012, 122 p.
115. **Ksenija Kisseljova**. Synthesis of aza-β^3-amino acid containing peptides and kinetic study of their phosphorylation by protein kinase A. Tartu, 2012, 104 p.
116. **Riin Rebane.** Advanced method development strategy for derivatization LC/ESI/MS. Tartu, 2012, 184 p.

117. **Vladislav Ivaništšev.** Double layer structure and adsorption kinetics of ions at metal electrodes in room temperature ionic liquids. Tartu, 2012, 128 p.
118. **Irja Helm.** High accuracy gravimetric Winkler method for determination of dissolved oxygen. Tartu, 2012, 139 p.
119. **Karin Kipper.** Fluoroalcohols as Components of LC-ESI-MS Eluents: Usage and Applications. Tartu, 2012, 164 p.
120. **Arno Ratas.** Energy storage and transfer in dosimetric luminescent materials. Tartu, 2012, 163 p.
121. **Reet Reinart-Okugbeni**. Assay systems for characterisation of subtype-selective binding and functional activity of ligands on dopamine receptors. Tartu, 2012, 159 p.
122. **Lauri Sikk.** Computational study of the Sonogashira cross-coupling reaction. Tartu, 2012, 81 p.
123. **Karita Raudkivi.** Neurochemical studies on inter-individual differences in affect-related behaviour of the laboratory rat. Tartu, 2012, 161 p.
124. **Indrek Saar.** Design of GalR2 subtype specific ligands: their role in depression-like behavior and feeding regulation. Tartu, 2013, 126 p.